UNIVERSITY OF OKLAHOMA

GRADUATE COLLEGE

DEVELOPMENT OF A STATE-WIDE VELOCITY PROFILE IN OKLAHOMA USING AMBIENT NOISE SEISMIC TOMOGRAPHY

A THESIS

SUBMITTED TO THE GRADUATE FACULTY

in partial fulfillment of the requirements for the

Degree of

MASTER OF SCIENCE

By

STEPHEN MARSH
Norman, Oklahoma
2018

DEVELOPMENT OF A STATE-WIDE VELOCITY PROFILE IN OKLAHOMA USING AMBIENT NOISE SEISMIC TOMOGRAPHY

A THESIS APPROVED FOR THE
CONOCOPHILLIPS SCHOOL OF GEOLOGY AND GEOPHYSICS

BY

_____
Dr. Norimitsu Nakata, Chair

_____
Dr. Xiaowei Chen

_____
Dr. Jacob Walter

ACKNOWLEDGEMENTS

I would like to acknowledge all those who have helped in the completion of this work. Firstly, Dr. Nori Nakata for his patient instruction, guidance, comments, and suggestions. Secondly to the other committee members for reviewing this work, Dr. Xiaowei Chen and Dr. Jacob Walter. To all those who have contributed through helpful insight: Raymond Ng, Jianhang Yin, Peiyao Li, Alex Arroyo, Francis Oyebanji, Zexuan Wang, Sebastian Alba, Rie Kamei, Andrew Thiel, Brett Carpenter, Pranshu Ratre, and Sean Lassiter. I would like to thank all my family and friends, especially my wife Sarah, who have encouraged and supported me through this entire process. Lastly, I want to make it known that Christ (God), who has enabled me to study His creation, deserves all credit and glory.

TABLE OF CONTENTS

List of Tables

Table Page

List of Figures

Figure Page

Abstract

Earthquakes have been a growing concern in the state of Oklahoma in the last several years and as a result, prediction of the ground motion, understanding of subsurface geological structure, and the estimation of accurate earthquake location are of utmost importance. This entails using a high-resolution velocity model with both lateral and vertical variations. The 3D S-wave velocity model in the entire state is determined using ambient noise seismic interferometry and tomography. Passive seismic data was acquired from broadband stations in multiple networks over eight years (2009-2016). We use seismic interferometry to extract wavefields between each possible pair of stations, for all components, and for each year. Then we estimate the dispersion curve of surface waves, such as Rayleigh and Love waves, and apply seismic tomography for building 2D velocity maps at each period. Finally, we convert the velocities into 3D S-wave velocities down to about 20 km depth based on the 1D surface-wave inversion. The velocity model clearly shows slower regions associated with basins of Oklahoma and faster regions associated with shallow basement in the northeast and various uplifts throughout the state.

Chapter 1: Introduction

In seismology, seismic velocities are some of the most used types of subsurface information. Understanding the velocities of different waves and in different locations can illuminate new information about different regions of the world as they relate to geological structure. Velocity is a function of elastic moduli and density, and also related to temperature, pressure, depth, and rock types. While layers generally extend horizontally in the subsurface, they are spatially heterogeneous. Understanding how seismic velocities change on a 3D scale is valuable and can be a useful starting point for earthquake seismology and geophysical exploration.

Induced seismicity has become a serious problem in Oklahoma due to the increase in seismicity in the state since 2009. Much of the increased seismicity has been linked with the increase in wastewater disposal, and since 2009 Oklahoma's annual rate of seismicity has increased by approximately 900-fold (Hincks et al. 2018). As fluid is injected into the subsurface, the number of seismic events has increased. The main source of induced seismicity in Oklahoma coincides with the increase of wastewater disposal wells beginning in 2008 (Keranen et al. 2018). Discerning which seismic events are naturally occurring, and which events are induced remains an inexact science. Little is known about the difference in seismic response of an induced versus naturally occurring event or if there even is a difference. Instead, induced seismicity is generally determined from a combination of injection volumes/rates, distance of events from wells, and the number of closely related events occurring in a short period of time. Oklahoma is an extreme case by the fact that Oklahoma has had over 2,500 magnitude 3.0 earthquakes between 2008

and 2017 (Keranen et al. 2018). On the other hand, Texas, California, Colorado, and North Dakota do not see the same number of earthquakes, the same magnitude, or on the same geographic scale (Keranen et al. 2018). This indicates that Oklahoma poses a unique problem as it relates to induced seismicity. One problem to understanding induced seismicity is the lack of detailed knowledge of basement structure, which is where most of the seismicity is occurring. The pathway from injection layers to basement (fluid migration) can be particularly important (Keranen et al. 2018).

To estimate the velocity model, we use ambient noise seismic interferometry and tomography. Seismic interferometry was first introduced by Aki (1957) and Claerbout (1968), who showed that the autocorrelation of a signal from a receiver can be interpreted as the receiver response of a virtual source at the same location. Seismic interferometry as applied in this study does not look at the autocorrelation of signals, but rather the cross-correlation of signals from different receivers. Various subsurface information can be extracted using ambient noise and applying cross-correlation (Shapiro et al., 2005; Lin et al., 2008; Nicolson et al., 2012, Nakata et al., 2015). After seismic interferometry has been applied, we can obtain surface wave dispersion measurements, and those surface wave velocities can be inverted to estimate 2D spatial maps at each period with seismic tomography. Seismic tomography uses the surface wave group or phase velocity measurement between receiver pairs to obtain surface wave velocities at specific geographic locations. There are theoretical/synthetic data examples giving an overview of seismic interferometry, one of which is Wapenaar et al. (2010). Other studies, such as Nicolson et al. (2012) showed how the methods of seismic interferometry can be used

with real data examples, in this case developing surface wave group velocity maps of the British Isles and Scottish Highlands using seismic interferometry and tomography. Examples of seismic tomography have been shown by Barmin et al. (2001), Zigone et al. (2015), Lin et al. (2009), and Rawlinson et al. (2014). Barmin et al. (2001) presents a method for seismic tomography that can be used on a local, regional, or global scale. Zigone et al. (2015) outlines data processing steps and tomographic results for the southern California Plate Boundary using noise-based Rayleigh and Love waves. Lin et al. (2009) portrays tomographic results using a phase front tracking method for much of the western United States with a 100 km resolution from the USArray Transportable Array. Rawlinson et al. (2014) outlines and shows many of the steps necessary for tomographic solutions and presents common methods for uncertainty determination of generated models.

In this study we present the results of ambient noise seismic tomography in Oklahoma. First, we give a brief overview of the recent seismic history of the state and the available data. Next, we go through the methods of data processing to extract virtual wavefields in Oklahoma and the group velocities of specific frequencies of those wavefields. These group velocities are then inverted into surface wave velocities for the state and subsequently depth converted to create a high resolution, 3D model for Vs velocity. Lastly the 3D velocity model is interpreted based upon known geology of the state of Oklahoma.

Chapter 2: Oklahoma Geology

Oklahoma has a rich geologic history. Some parts of the state, mainly southern Oklahoma where most of the basins are bounded, have been above and below sea level, with various regions experiencing major folding and faulting resulting in the structures seen today (Johnson 2008).

The Anadarko Basin and Arkoma Basin are two examples of sedimentary basins, figure A9. The Anadarko Basin is located in southwest Oklahoma and is characterized by a zone of thrust faults most notably the Meers Fault which contributes to the structure of the Wichita Mountains (Perry Jr. 1989). The Anadarko Basin is also known as one of the deepest sedimentary basins in North America (Perry Jr., 1989). Due to deeper sedimentary layers, it is expected that this region in Oklahoma is seismically characterized by slower velocities at equivalent depths compared with other areas of Oklahoma. In fact, the northern part of state differs from the south in that most of the sedimentary layers are relatively thin and horizontal (Johnson 2008 and Crain et al. 2018). This means that granitic basement is more shallow in the north as opposed to the south (Crain et al. 2018).

The Arkoma basin is another large sedimentary basin in southeast Oklahoma (Johnson 2008). Seismic velocities should be slower than the northern part of the state for the same reason that the Anadarko Basin is slower. The sedimentary layers of the Arkoma Basin are found at depths similar to those in the northern part of Oklahoma where granitic

basement is located. The Anadarko and Arkoma Basins are the major geologic features of note in Oklahoma that are expected to play a major role in seismic velocity estimation.

Oklahoma is also a very complex state structurally. Marsh et al. (2016) developed a fault map compiled from published literature which captures the entire state, figure A24. Major fault structures include the Nemaha Uplift, which has considerable throw in northern Oklahoma, the Meers Fault in southwestern Oklahoma, which has a history of larger magnitude events, and many thrust fault systems in southwestern Oklahoma. In fact, the Southern Oklahoma Aulacogen is a failed continental rift and is largely composed of igneous material (Whitmeyer et al. 2007). This part of the state has been known to produce large earthquakes in recent geologic history along the Meers Fault (Luza et al. 1987).

Chapter 3: Data

We use continuous seismic data recorded by broadband stations in Oklahoma, Kansas, Texas, and Arkansas (Figure 1). We choose these stations to focus on estimation of the velocities in Oklahoma. The stations within Oklahoma provide information in central Oklahoma, while the stations in Kansas, Texas, and Arkansas help provide high resolution to the border regions of Oklahoma. Using all the stations together helps to increase the station coverage with high spatial density. All data is available via the Data Management Center of the Incorporated Research Institute in Seismology (IRIS DMC). The data used in this study are from the year 2009 to 2016. We remove instrument response and resample all recorded data to 0.05s (20 Hz) and store it separately by day. This sampling frequency is chosen because this frequency is still high enough for seismic tomography explained below, and computation time and memory requirements are significantly reduced which allows for faster and more efficient processing. Each file refers to a specific day of recording and contains all stations which recorded on that day. Due to 20 Hz sampling frequency, each receiver in each file contains 1,728,000 samples (86400 s * 20 Hz).

The number and locations of stations have changed from year to year (Figure 1). In 2009 there were 41 stations active and used by this study, and it has since increased to 189 stations in 2016 (Figures A1-A8). Most of the stations are located in north-central Oklahoma after 2013. This is because most of the seismicity is occurring in north-central Oklahoma and stations have been installed there to better capture the signal. For our study, these dense receivers are important for estimating subsurface velocities with higher

spatial resolution. The Transportable Array (TA) of USArray passed through Oklahoma between 2009 and 2012. The TA array provides a complete and uniform coverage of the state and combining it with the local stations gives more localized coverage in the state.

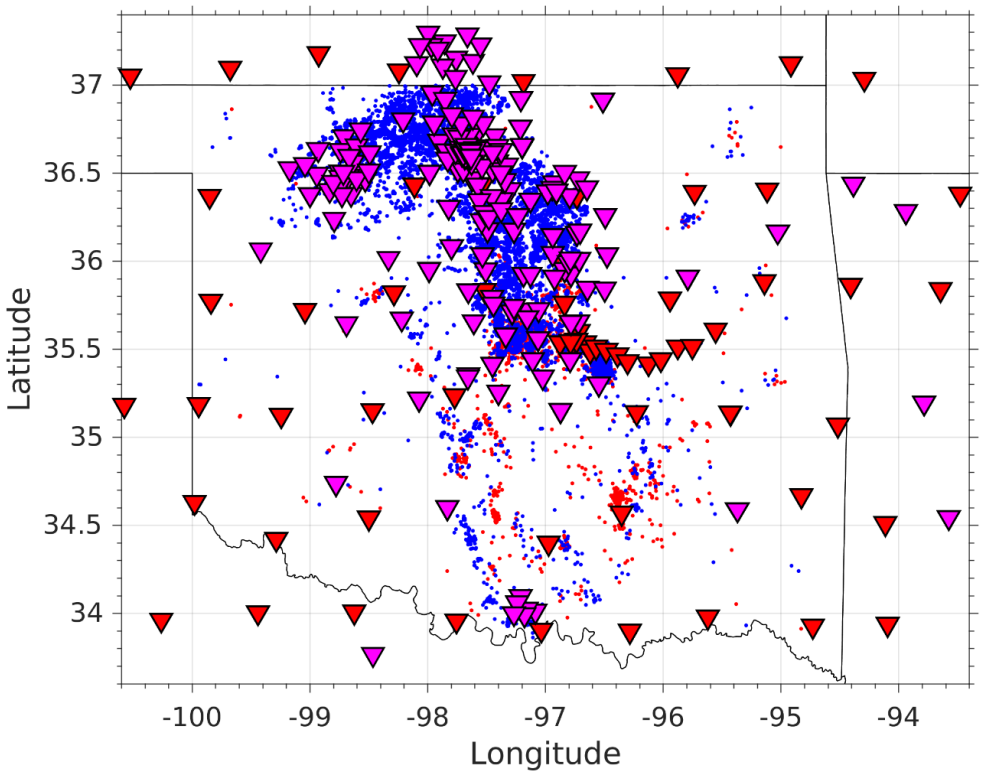

Figure 1: Station Coverage from 2009 - 2016. Red triangles represent the location of each individual station from 2009 - 2012. Purple triangles represent stations from 2013-2016. Red dots represent seismicity occurring between 2009-2012 and blue dots represent seismicity from 2013-2016.

Chapter 4: Methodology

In this study, we start with ambient noise data and apply (1) seismic interferometry, (2) dispersion curve analysis, (3) seismic tomography, and (4) depth conversion to the data. Each of these four steps contains many processing steps within, and they ultimately allow us to take the recorded data and obtain meaningful 3D velocities throughout the state of Oklahoma.

4.1. Seismic Interferometry:

Ambient noise seismic interferometry is a method which uses passively recorded seismic signal at multiple receiver locations to generate virtual wavefields that resemble Green's function between those receivers. The idea is implemented through cross-correlation of two signals with each other, the result of which theoretically represents the wave propagation from one receiver to the other. Specifically, long time series are used in the cross-correlation of ambient noise to estimate the Green's function (Das et al. 2016). We can improve the signal-to-noise ratio (SNR) by stacking multiple long-time series together. The long-time series captures more information about the signal that is being recorded at each station. Stacking those signals improves the SNR because it amplifies the coherent signal and suppresses random noise. The amplification and diminishing of signal and noise is due to the seismic traces constructively and destructively interfering during the stacking process. The stacked signal, which shows the arrival times of dominate waves at each receiver, is then cross-correlated which provides us with the estimated Green's function as discussed above. The signal that destructively interferes, is reduced and plays little part in the acquired wavelet. One benefit to using this method is

that the position and source signature of the true noise source or the propagation velocity does not need to be accurately known (Wapenaar et al. 2010). We can treat the cross-correlated signal as if it originated at one receiver and was recorded at the other.

When we record seismic data, we know the exact location of the recording stations. The rest of the information is contained within the signal itself, such as arrival time, frequency content, and others. It is important to know the time it takes for a wave to propagate from one receiver to the next. Velocity is measured as distance over time, and because we already know the location of the receivers we can infer the distance based upon a likely path of propagation. The only thing left is knowing the time it takes for signal to travel from the source receiver to the recording receiver. It is through retrieving the Green's function that we can obtain the arrival time information and frequency content, which helps determine path of propagation and therefore distance.

In seismic interferometry, we cross-correlate wavefields recorded at receiver 1 (r_1) and receiver 2 (r_2). Equation 1:

$$C(\tau) = \int_0^T r_1(t) r_2(t+\tau) dt \,, \tag{1}$$

where $C(\tau)$ is the cross-correlated wavefield after integration over time T, t is the recording at receiver 1, and τ time shift between r_1 and r_2. The key to obtaining a useful estimated Green's function is correlating receivers over as many noise sources as possible, which increases our signal to noise ratio. It is therefore valuable to have a long period of recording in order to incorporate as many noise sources as possible. This can most easily be accomplished by averaging all recording time over the interval T.

Averaging will ensure that the dominate noise direction is amplified for the cross-correlation. When averaging for both receivers, the signal-to-noise ratio is improved for both individual receiver wavelets and subsequently the wavelet after cross-correlation. For seismic interferometry to work well the ideal case is to have an equal distribution of noise sources coming from all directions. Unfortunately, nature does not follow the ideal case. Instead noise is unequally distributed and will not provide adequate coverage to extract a useful wavefield between receivers when only recording over a short time frame. If the signal is averaged over a long period of time, many noise sources and directions are now represented as having occurred within a shorter time frame, providing the adequate noise distribution (Snieder 2004, Das et al. 2016). Figure 2 below is a visual example of how cross-correlation is useful.

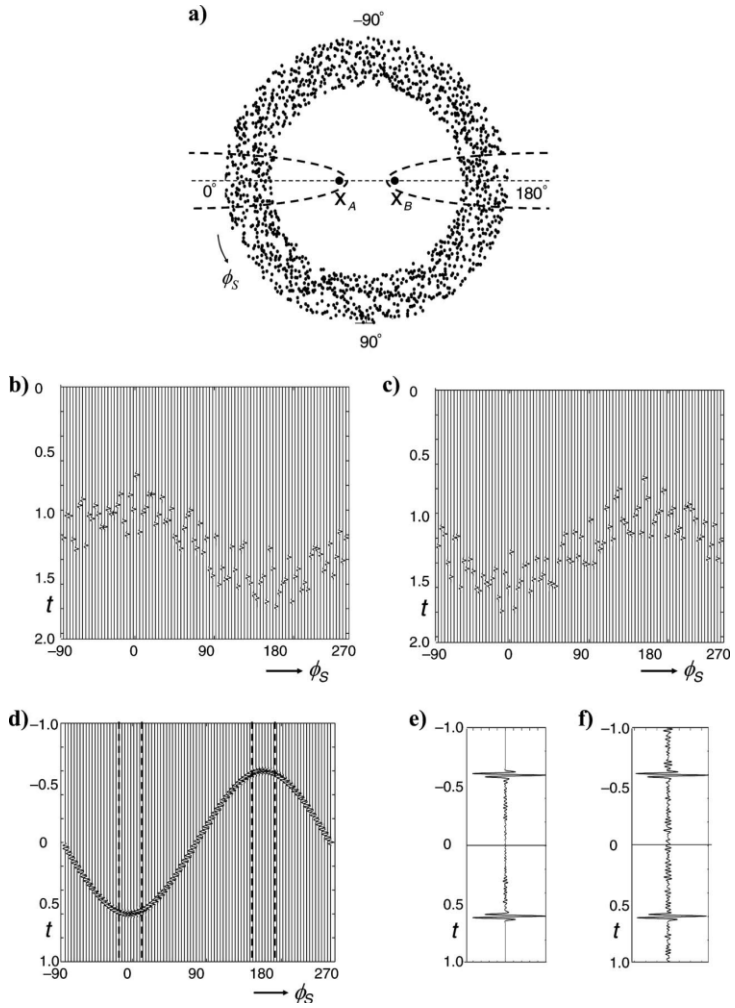

Figure 2: Synthetic example of noise correlations. Wapenaar et al. (2004)

Figure 2a shows two receivers, X_A and X_B, passively recording signal generated by the noise sources denoted by all other black dots. Figure 2b and 2c show the response of the noise sources by their location (-90-270°) at receiver X_A and X_B respectively. Figure 2d shows the cross-correlated response of the wavelets at both receivers. Each trace is representative of the wavefield between receivers for that particular source. Figure 2e is the summed traces from d, showing the region of highest constructive interference in the cross-correlated signals, thereby retrieving the estimated Green's function between receivers. Figure 2f is a single cross-correlation of simultaneously acting noise sources, whereas b-e show the responses of non-simultaneous noise and subsequent cross-correlation.

4.2. Wave-type Extraction:

In general, seismic signals are recorded in three different components (e.g., the vertical, north-south, and east-west components). Different components are often more or less sensitive to various types of waves. The P-Wave (Primary Wave), for example, is a compressional wave and is more easily captured by the vertical component. The S-Wave

(Secondary Wave) is a shear wave and is usually more easily captured by the horizontal components (north-south or east-west). Both the P-wave and the S-wave are categorized as body waves. Surface waves are another category of waves that are generally seen on all components, although the best recording can change from component to component depending on the wave at that given time. Comparison of the arrival times of the waves tell us that P-waves are fastest, followed by S-waves, and then surface waves are the slowest of the wave types. Just like body waves, surface waves can be broken into two types of waves, Rayleigh waves and Love waves. Love waves travel faster than Rayleigh waves and have a different motion of propagation. Love waves have a combination of vertical rolling and horizontal shear motion while Rayleigh waves propagate in an elliptical fashion. Surface waves only propagate in the near surface, whereas body waves can travel through most of the earth regardless of depth. However, S-waves do not propagate through liquid mediums and therefore do not propagate through the outer core of the earth. For the purposes of our research we use surface waves for interferometry and tomography because doing so provides us with high enough signal-to-noise ratio to know when the waves arrive. Body waves do not always have high enough amplitude in ambient noise to know when they arrive exactly. Figure 3 below portrays an example of the relative amplitudes of Rayleigh waves and S-waves in a cross-correlated, and stacked station gather based on interstation distance (Poli et al. 2012).

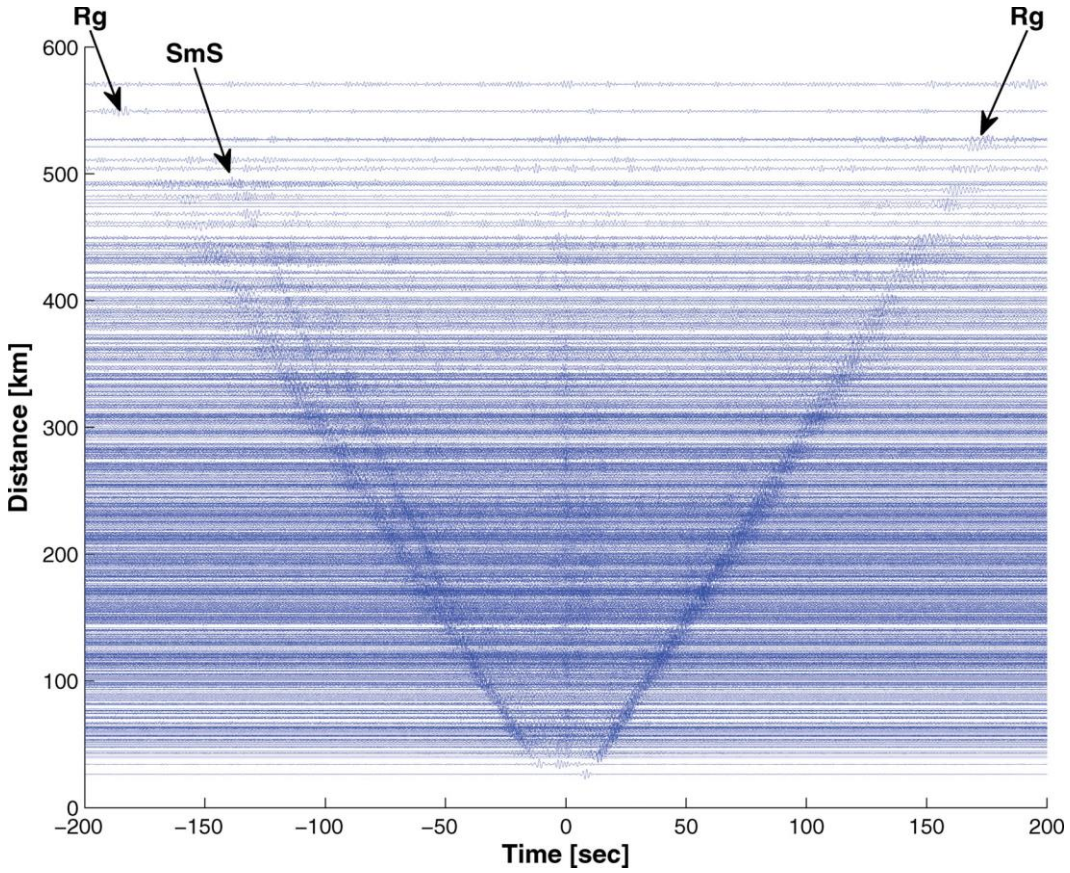

Figure 3: Cross-correlations of RR components showing arrivals of Rayleigh waves (Rg) and S-waves (SmS). Poli et al. (2012)

Data must be rotated from 3-component data into 9-component data, using a rotation matrix, to prepare for tomographic surface wave inversion. This rotation first involves rotating the horizontal components (NE) in to the direction of each receiver pair (radial, R, and transverse, T; Nishida et al., 2008). Then, the cross-correlation between each of these rotated components provide the 9-component data: ZZ, ZR, ZT, RR, RZ, RT, TT, TZ, TR. When we assume anisotropy is weak or nonexistent, ZZ, ZR, RZ, and RR components contain the Rayleigh wave information, and TT for Love waves. We use these components for the analyses below. Surface waves are used instead of body waves because of the higher amplitudes. For this reason, it is easier to pick the arrivals of surface

waves in ambient noise, than it is for body waves. From there body wave velocities can then be inferred from surface wave velocities. It is much harder to find body wave velocities in ambient noise without the use of surface waves. Additionally, each cross-correlated receiver-pair's signal is stacked according to the rotated component to improve signal-to-noise ratio and obtain the arrival time at the recording receiver of the virtual signal from the virtual source. The distance between source and receiver is known because one receiver in the pair acts as a virtual source. The arrival time of the virtual wave is also known due to the process of seismic interferometry described above. Combining these two pieces of information, we can obtain velocity information using dispersion curve analysis.

4.3. Dispersion Curve Analysis:

Developing a 3D velocity model is not as simple as using the distance between stations and dividing it by the virtual signal's observed arrival time. It is extremely helpful to obtain velocity estimations for different depths. This is done through group velocity measurements based on the period of the surface wave. This is called surface wave dispersion analysis (Bensen et al. 2007). Table 1, provided by Levshin et al. (1989), gives a good indication of surface wave frequencies and their associated depth sensitivity.

frequency (Hz)	period (sec)	wavelength (km)	phase velocity (km/sec)	depth of penetration (km)	application
10-50	0.02-0.1	0.002-0.05	0.1-0.5	0.020	Static Corrections, Civil Engineering, Archeology
1-5	0.2-1	0.15-1.5	0.1-1.5	0.2	Static Corrections, Upper Sediments Studies
0.1-0.2	5-10	7-30	2-3	5	Sedimentary Basins Studies
0.03-0.1	10-35	30-100	3.0-3.5	40	Crustal Studies
0.003-0.03	35-350	200-1000	4-5	300	Upper Mantle Studies

Table 1: Surface Waves in the Earth's Studies Levshin et al. (1989).

Based upon Table 1, frequency ranges from 0.03-1 Hz should be sensitive to upper sediments, sedimentary basins, and crustal structure. Frequency is the inverse of period (s). This frequency range is equivalent to obtaining dispersion measurements in 1-33 second periods. To find the dispersion measurements we follow the steps outlined by Bensen et al. (2007).

1: Convert correlated wavefields to frequency domain using Fourier transform.

2: Consider only the analytical signal portion of the cross-correlated signal.

3: Bandpass Gaussian filters with center frequency ω_0.

The result of these steps provides us with two main parts (Bensen et al. 2007), where ω_0 refers to center frequencies:

$$|A(t,\omega_0)| \quad and \quad \emptyset(t,\omega_0)$$

Our main concern is with $|A(t,\omega_0)|$ which helps to provide us with group velocity measurements. The other part, $\emptyset(t,\omega_0)$, is useful for looking at phase velocities. Looking at $|A(t,\omega_0)|$ provides an envelope function, the peak of which corresponds with our group velocities (Bensen et al. 2007). The peak of the envelope function is tracked for

each frequency and stored as the group velocity measurement. This provides the following equation to represent group velocities (Bensen et al. 2007) where r is the interstation distance, τ is time, and ω_0 is instantaneous frequency:

$$U(\omega_0) = \frac{r}{\tau(\omega_0)}$$

Once enough group velocity measurements are obtained, we can then use these as velocity input for our surface wave tomographic inversions.

4.4. Tomographic Inversion:

Our main goal in this research question is to be able to determine seismic velocities in different areas of the state and at different depths. Using the arrival times from the virtual wavefields only gives us the average velocity as the wave travels between the two stations. We want to determine the exact velocities at each point along the path of propagation. To do this, we must perform a tomographic inversion which requires a starting velocity model. Group velocities are also used from the dispersion curves and a final model is developed through an iterative process which attempts to reconcile the observed velocities from the dispersion curves and the starting model. The inversion method we used was provided by Barmin et al. (2001). Regularization within this method, as described by Barmin et al. (2001), "places constraints upon the model amplitude, magnitude of perturbation from a reference state, and on the amplitude of the first and/or second spatial gradients of the model." The inversion scheme recognizes regions of poor coverage and applies user defined regularization parameters which results in a smoother model. Regularization is spatially variable and adaptive and therefore will not affect

regions of high data coverage the same as regions of poor coverage. This is done by minimizing the penalty function during the inversion.

For the purpose of our research, we choose to do isotropic velocity inversions due to the simplicity of the developed model. However, anisotropic tomographic inversions can be done using the method described by Barmin et al. (2001). Also, there are a couple key parameters to be aware of in any tomographic inversion: grid size, damping, and smoothing. The region of inversion is first broken up into a grid of nodes that are relatively evenly spaced. Damping and smoothing parameters play key roles in how much weight to give the initial model when considering regions with low ray path density and how surrounding nodes may affect the velocity selection at a given node.

To determine what size of grid spacing to use, we choose based upon desired resolution and the computation time required for that inversion. The more grids (i.e. small grid size), the longer it will take to run the inversion. There is also the issue of data density. As with any model inversion we have a set of unknowns, these are the velocity values at each grid node. To adequately solve for those values, we need to have enough station-receiver pairs to provide multiple ray paths though each grid. This will help ensure that the values provided during the inversion match well with the observed data. Therefore, our grid size selection must be made with the knowledge that we cannot have more grids than ray paths, otherwise our inversion will be ill-posed, and our result will not be trustworthy.

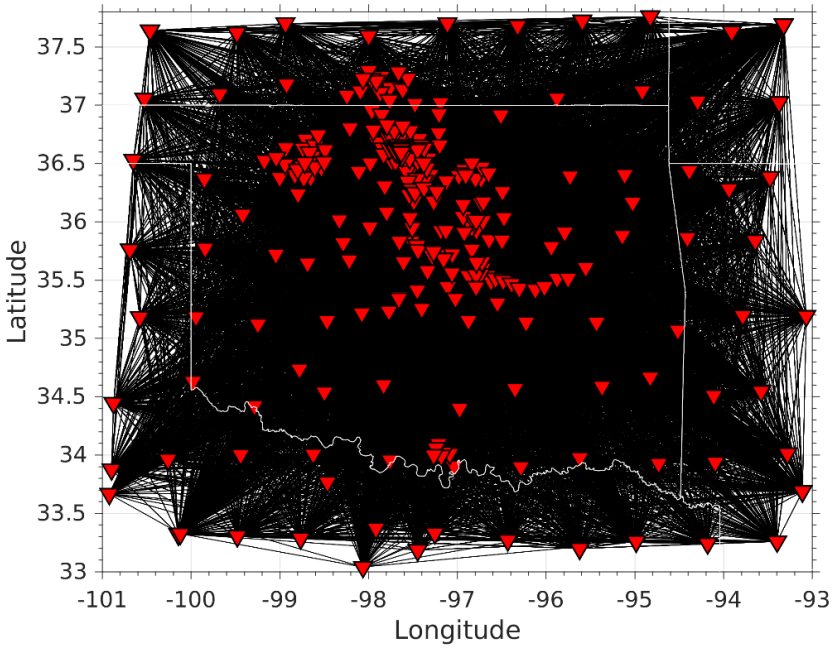

Figure 4: Showing each ray path between stations. Red triangles show location of each station (2009-2016). Each black line shows the path between 2 receivers.

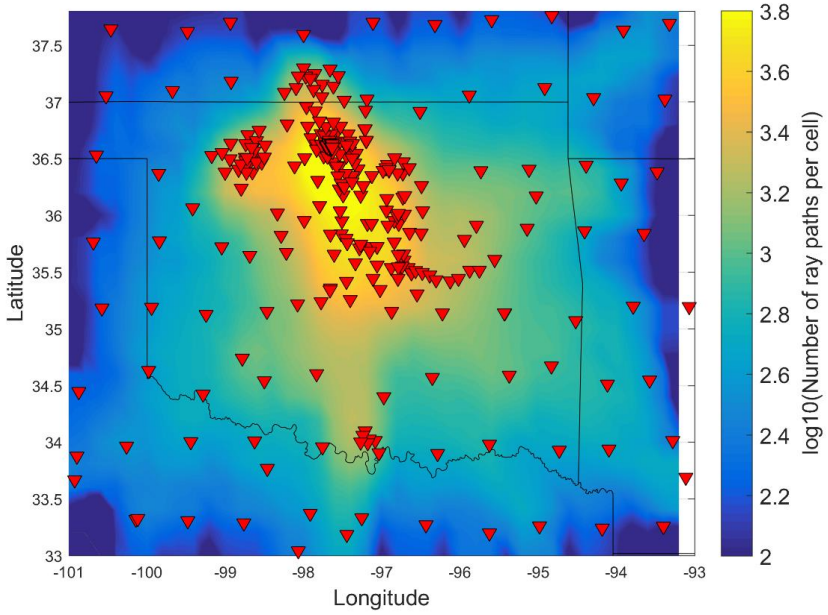

Figure 5: Ray-path density map. Color scale based on the number of ray paths per cell on a logarithmic scale. North-central region shows extremely high density.

Damping and smoothing parameters are chosen based upon experimental results. We find stable damping and smoothing parameters to solve the inverse problem by minimizing

the misfit and also increasing the resolution. Note that the inversion assumes that the final velocity model is a smoothed version of the initial inverted model (Barmin et al., 2001), and we do not choose the parameters only based on minimizing the misfit to avoid over-fitting as similar to Mordret et al. (2013). This means the parameters are chosen to ensure that the final model has a higher level of data fit, contains high resolution, and is visually geologically reasonable.

Each component (TT, ZZ, RR, RZ, ZR) is selected to run through the same inversion parameters stated above for periods 1-25 seconds. This gives us many different velocity maps for both Rayleigh and Love waves that can then be converted to depth and inverted to find Vs velocities.

4.5. Depth Conversion:

Seismic velocities are not very useful unless they can be easily understood and used. In the methods described above velocity is represented as either Love wave or Rayleigh wave velocities with respect to period. Velocity in the subsurface is much more easily understood when related to depth instead of period. Therefore, this section focuses on converting the surface wave velocities into Vs velocities that are represented by depth and not by period. Another inversion method developed by the Earthquake Center at Saint Louis University was used to determine velocity at depth (Herrmann 2013).

This method takes dispersion measurements of Love and Rayleigh wave velocities and inverts them to Vs velocities. Herrmann's method follows the tomographic inversion

described above because it can easily be applied to each latitude and longitude point across the state of Oklahoma. The model, which is generated through the tomographic inversion, is essentially an estimated dispersion curve at each geographic point. Instead of dispersion velocities being represented by period for a station-receiver pair, the velocities are by period with respect to a specific geographic location. Herrmann's (2013) method allows for the generation of a layer model. The model is then iteratively solved for Vs velocities for each specified layer with given thickness. This process can be done for each geographic point, completely independent of all other locations. Once each location has been solved, it can be combined into a 3D volume where velocity is given at each possible geographic location (longitude and latitude) and at depth.

Chapter 5: Results

5.1. Dispersion Curves:

One of the first steps performed in estimating seismic velocities is to measure the dispersion of a wavefield. Figure 6 below is one example of many dispersion measurements being performed on a specific station pair. Similar measurements are taken for each possible station pair and the group velocity is selected for each period (1-25 seconds). Figure 6 shows each of the five components and the corresponding group velocity measurements. These components will help highlight different velocities for both types of surface waves, Love and Rayleigh. Ideally the measurements would be a nice smooth curve for all five components, but visibly that is not always the case. Sometimes there is jump in the velocity, either up or down, which is uncharacteristic and should be used with caution. The green curve, which measures the peak of the dispersion envelope, provides the group velocity values.

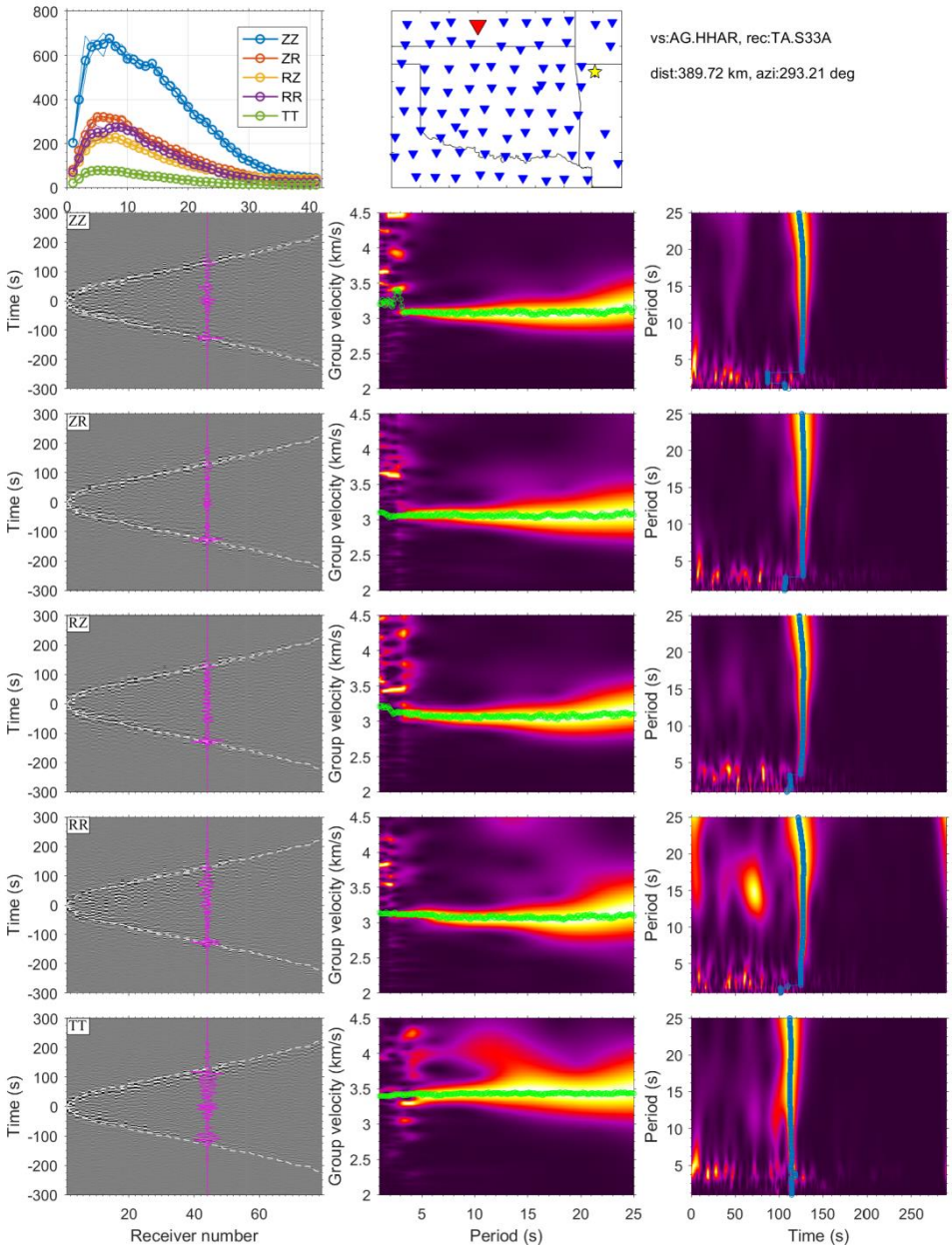

Figure 6: First column shows the virtual shot gather between station pairs. The star in the map in the top of the second column is the source station and the red triangle is the receiver station. The second column shows the group velocity measurements of period 1-25 second. Blue and green lines are the measured velocity and is trusted when lines are nearly identical. The third column shows the dispersion measurement as it relates to period and to time of recording of the virtual signal.

5.2. Tomography:

The tomographic inversion is done using the group velocity measurements and the output is surface wave velocity measurements for a specific component and period. The result is a state-wide map of velocities for each unique solution. The solutions shown below are the results of inversion with all the components ZZ, ZR, RZ, RR, TT, and with periods of 5, 10, 15, and 20 seconds. It is apparent that slower velocities are seen in red and faster velocities are denoted by blue. As discussed above, the regions of the Arkoma and Anadarko basins exhibit slower velocities than the northern part of the state, particularly the northeast. There is also a trend of increasing velocity as period increases. This is because depth sensitivity increases with the period, meaning longer periods measure velocities at deeper depths which are generally faster than shallow depths.

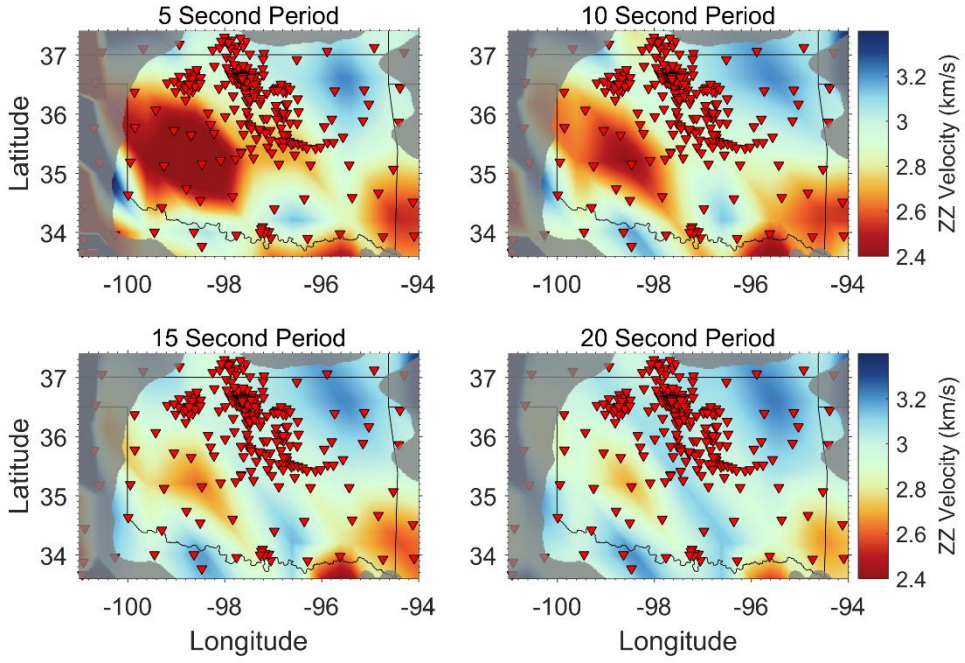

Figure 7: Showing velocities after tomographic inversion for the 5, 10, 15, and 20 second periods for the ZZ component. Gray overlay indicates regions of less than adequate ray coverage for tomographic inversion and results are considered unreliable.

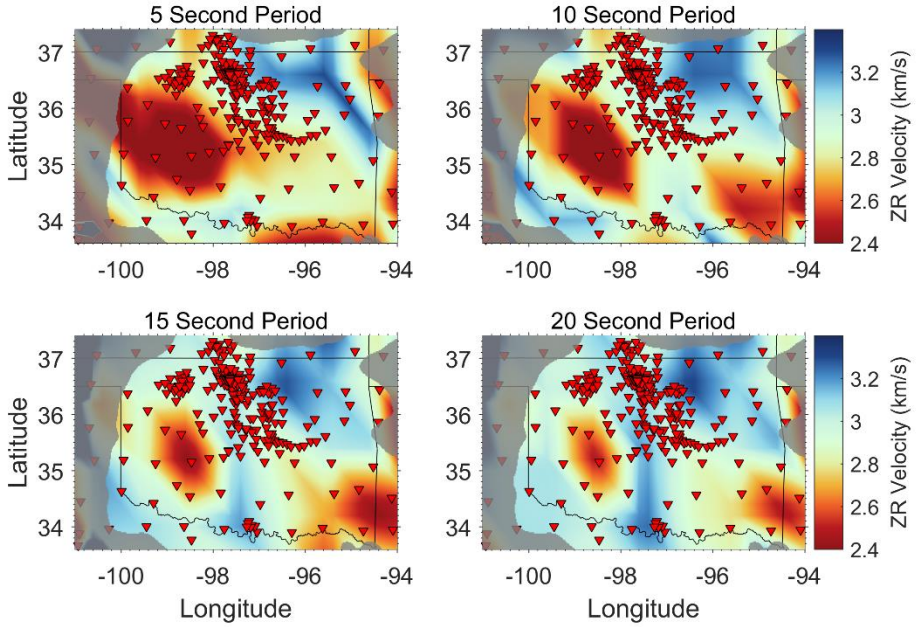

Figure 8: Showing velocities after tomographic inversion for the 5, 10, 15, and 20 second periods for the ZR component. Gray overlay indicates regions of less than adequate ray coverage for tomographic inversion and results are considered unreliable.

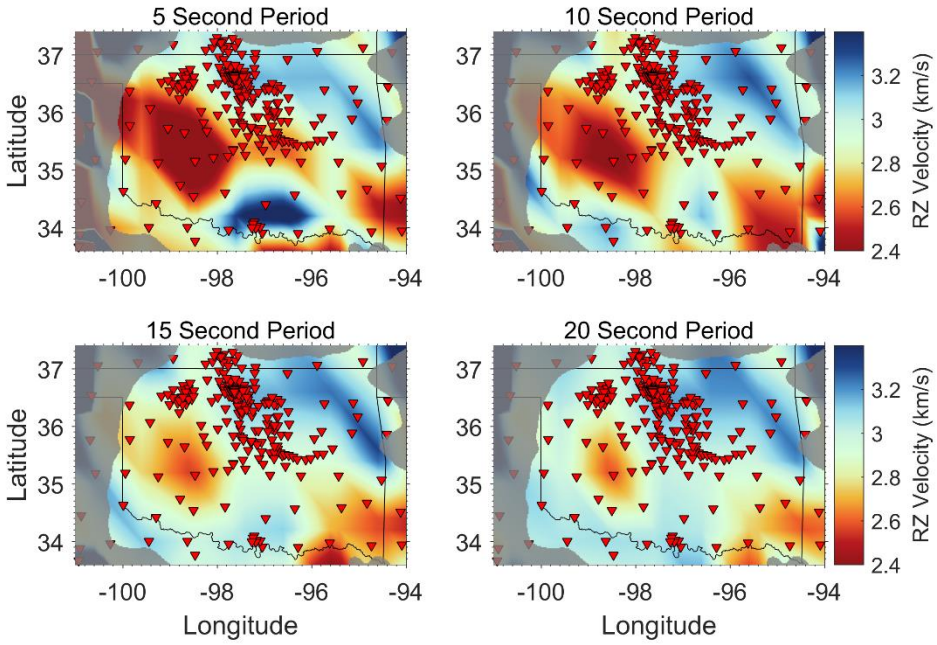

Figure 9: Showing velocities after tomographic inversion for the 5, 10, 15, and 20 second periods for the RZ component. Gray overlay indicates regions of less than adequate ray coverage for tomographic inversion and results are considered unreliable.

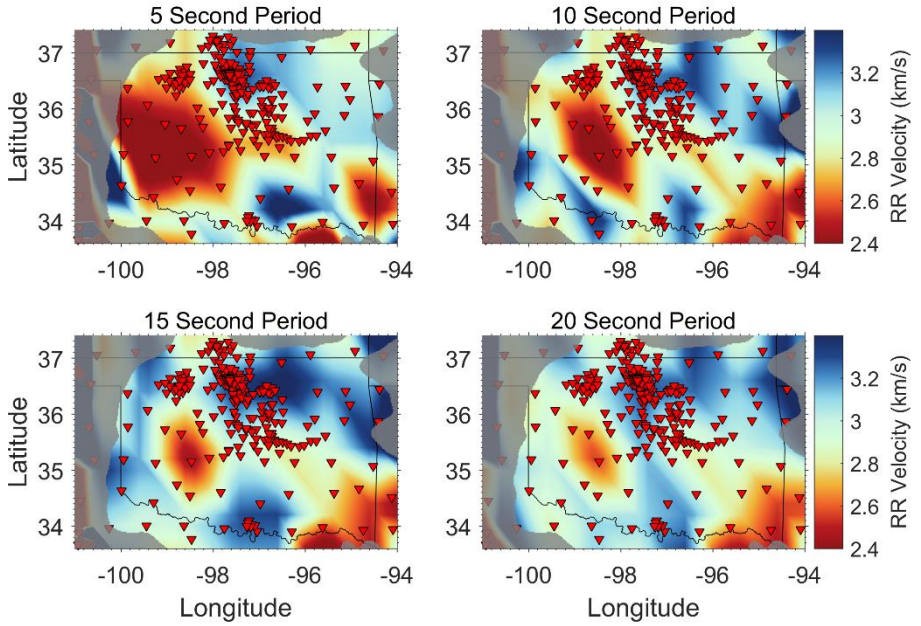

Figure 10: Showing velocities after tomographic inversion for the 5, 10, 15, and 20 second periods for the RR component. Gray overlay indicates regions of less than adequate ray coverage for tomographic inversion and results are considered unreliable.

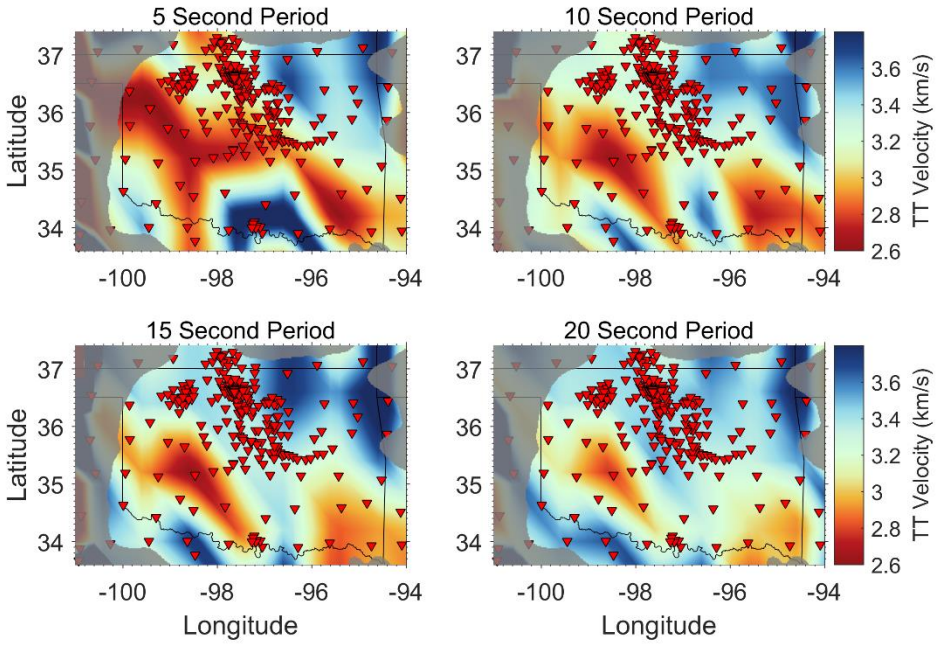

Figure 11: Showing velocities after tomographic inversion for the 5, 10, 15, and 20 second periods for the TT component. Gray overlay indicates regions of less than adequate ray coverage for tomographic inversion and results are considered unreliable.

In addition to a state-wide tomographic inversion, a secondary inversion was done using only the dense receiver array for each component. These secondary inversions used an isotropic grid cell size of 0.6 degrees, increasing the resolution of the inversion for that region. This is only possible in this region due to the dense coverage. The state-wide inversion uses an isotropic grid cell size of 1.0 degrees, which has lower resolution, but produces geologically reasonable results with ray path density available in all parts of Oklahoma. Figures 13-17 below show the inversion results of the dense receiver region.

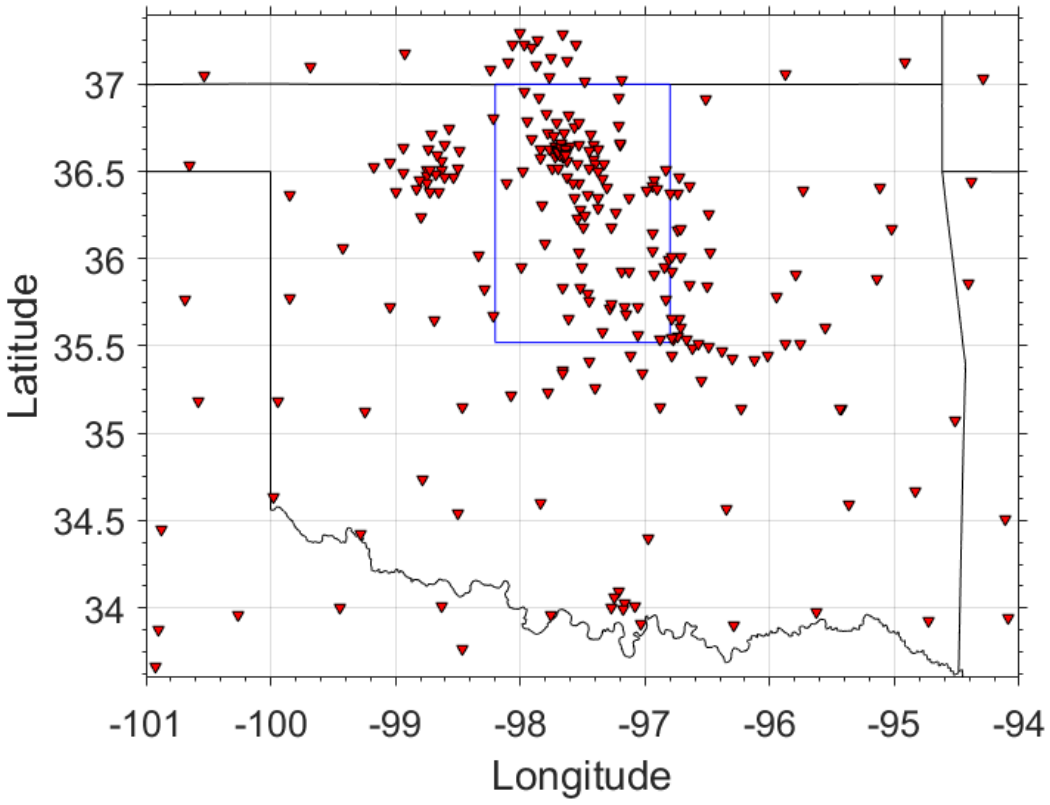

Figure 12: State of Oklahoma, with receiver coverage, and blue box outline is the location of the dense receiver tomographic velocities shown in figures 13-17.

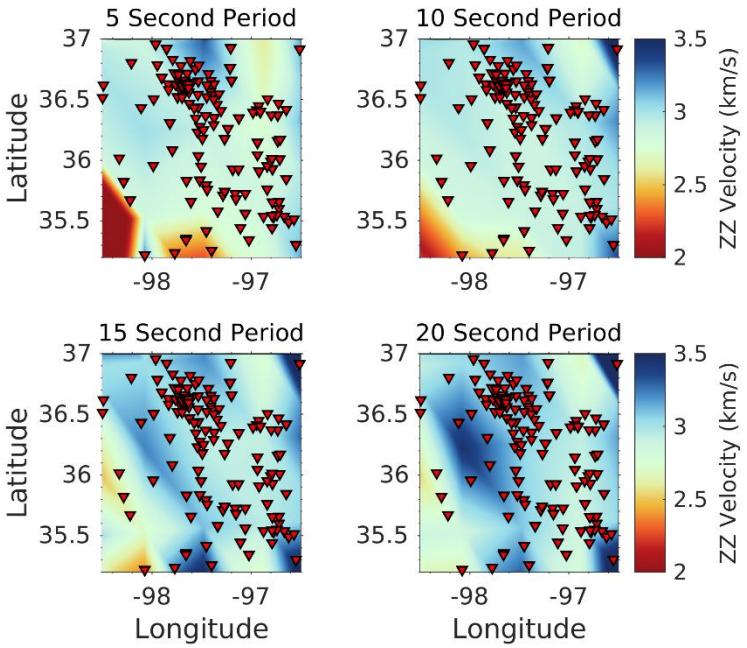

Figure 13: Showing velocities after tomographic inversion for the dense receiver region for 5, 10, 15, and 20 second periods for the ZZ component.

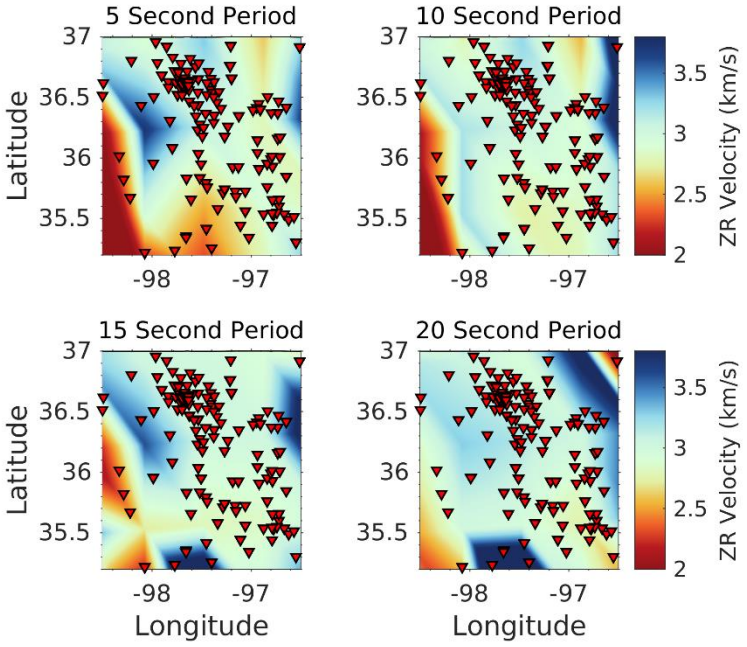

Figure 14: Showing velocities after tomographic inversion for the dense receiver region for 5, 10, 15, and 20 second periods for the ZR component.

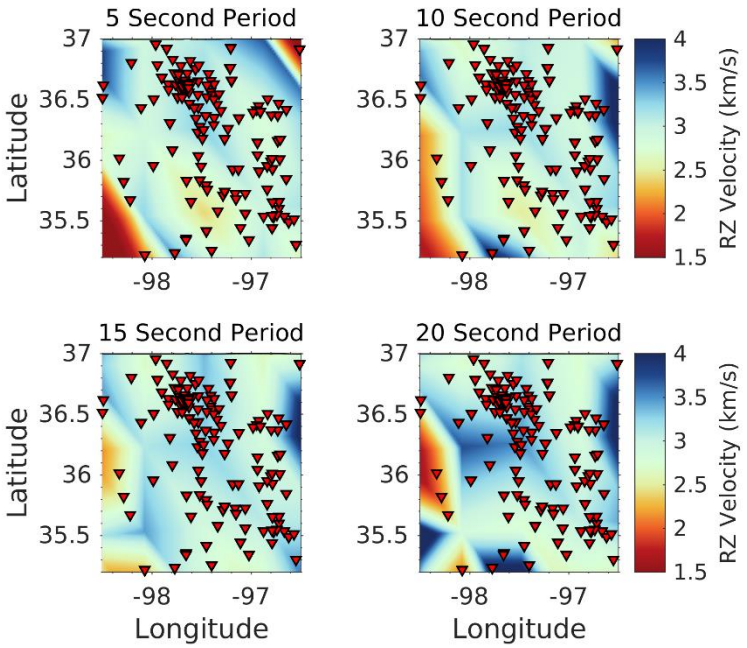

Figure 15: Showing velocities after tomographic inversion for the dense receiver region for 5, 10, 15, and 20 second periods for the RZ component.

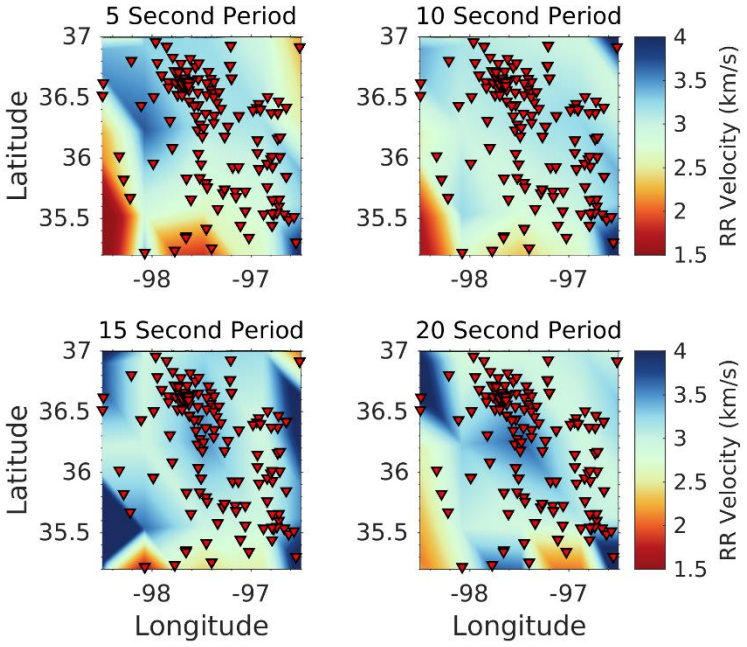

Figure 16: Showing velocities after tomographic inversion for the dense receiver region for 5, 10, 15, and 20 second periods for the RR component.

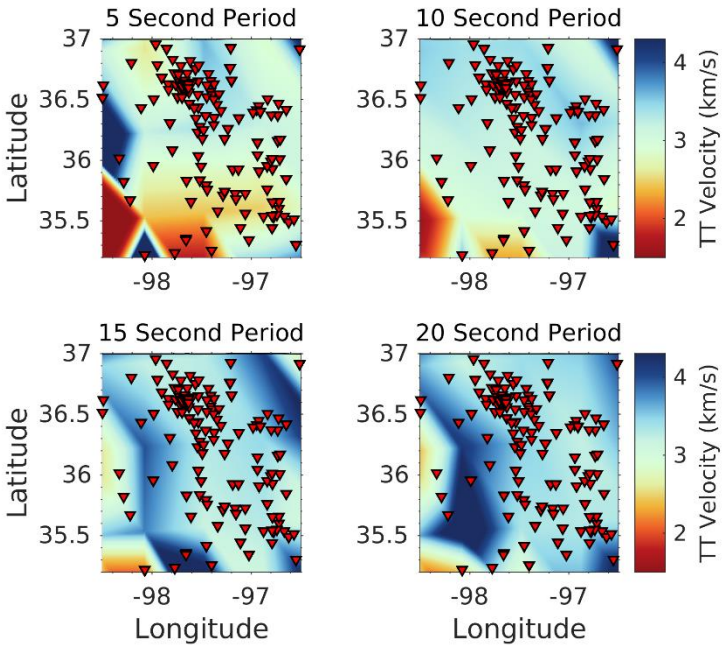

Figure 17: Showing velocities after tomographic inversion for the dense receiver region for 5, 10, 15, and 20 second periods for the TT component.

5.3. Model Improvement:

During the inversion process, each grid cell is assigned a velocity value. One of the most important things is to understand how accurate these estimated values are. Figures 18 – 22 show the starting model and final model residuals. These are indicative of the model's similarity to real observed data; the taller and thinner the histogram is, the more accurate the model. Another indication of model improvement is by comparing the RMS (root mean square) values of the inversions. The smaller RMS value indicates that it is closer to real observed data, and therefore a better model.

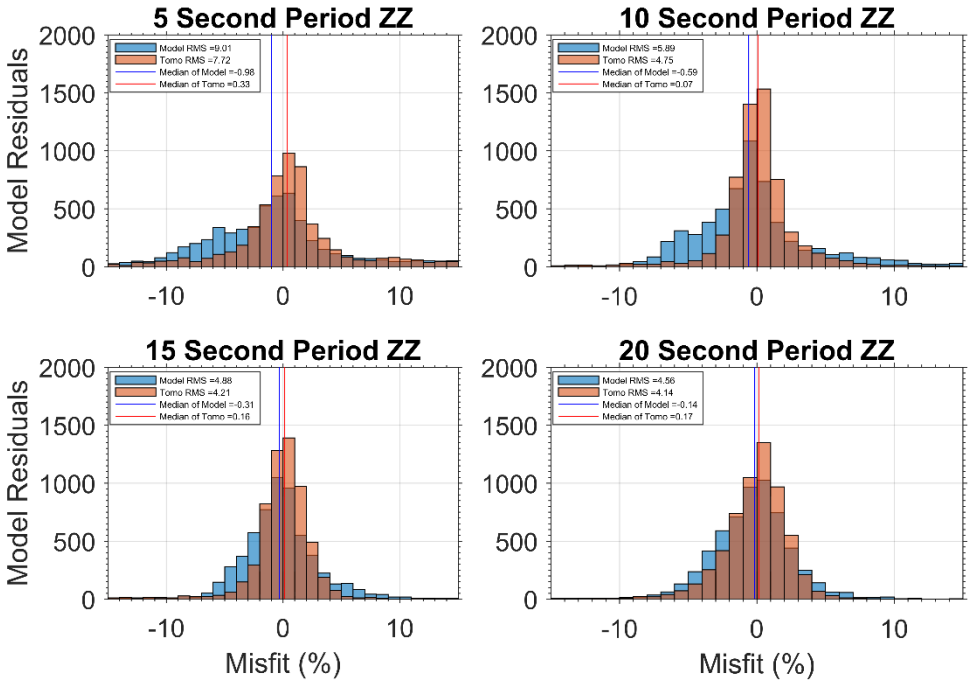

Figure 18: Histograms showing starting model (blue) residuals and tomographic model (brown) residuals.

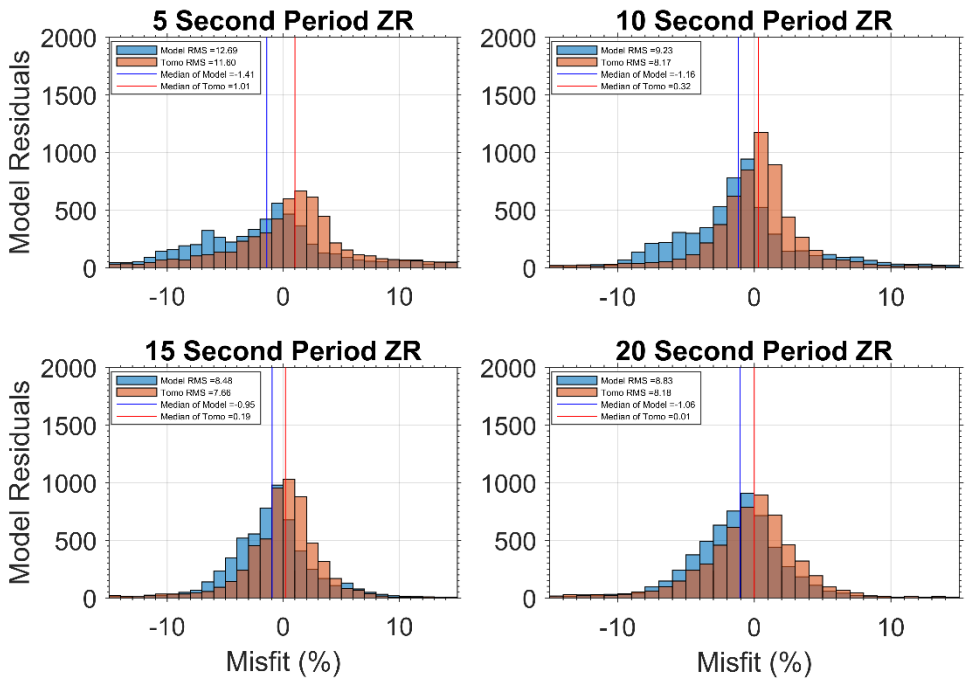

Figure 19: Histograms showing starting model (blue) residuals and tomographic model (brown) residuals.

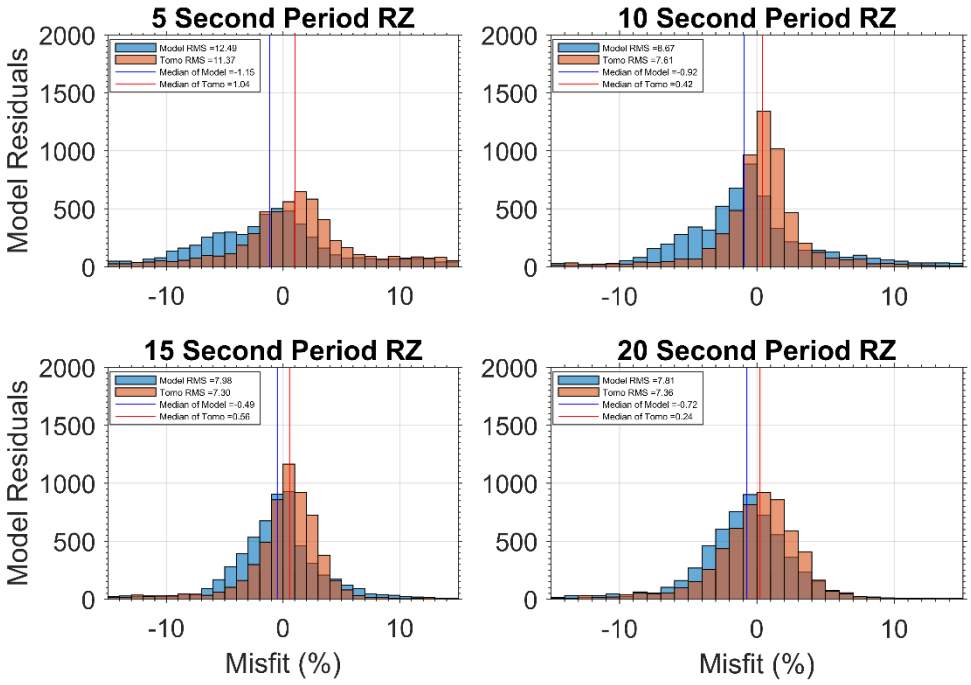

Figure 20: Histograms showing starting model (blue) residuals and tomographic model (brown) residuals.

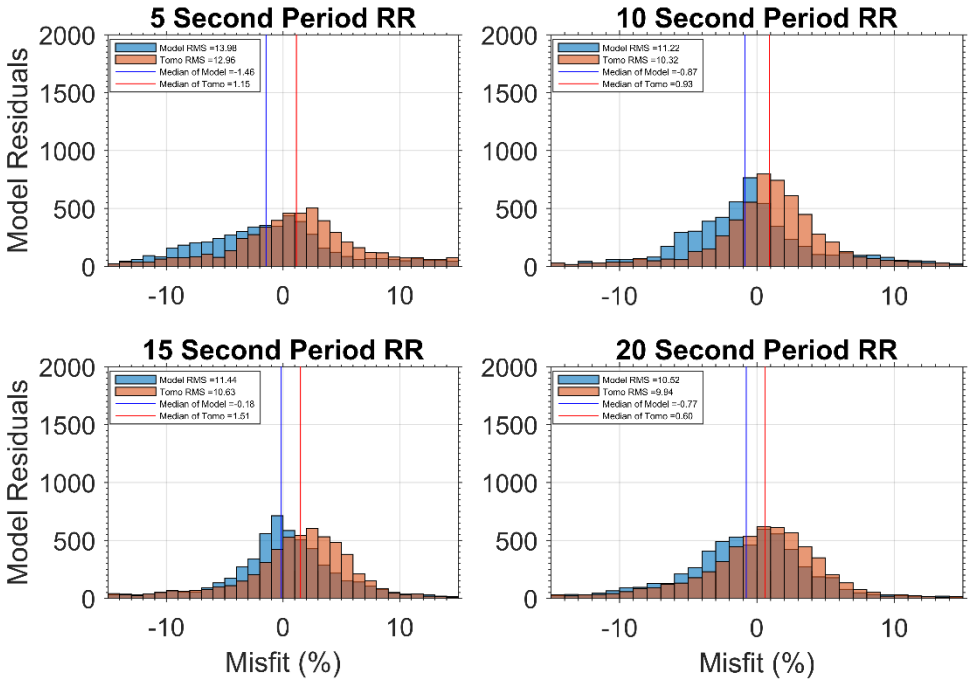

Figure 21: Histograms showing starting model (blue) residuals and tomographic model (brown) residuals.

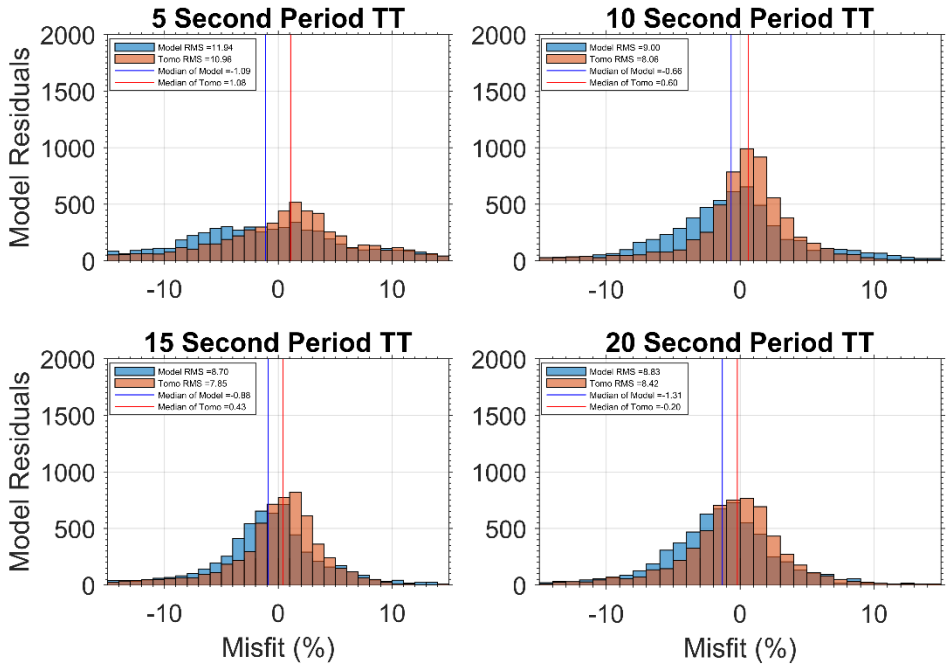

Figure 22: Histograms showing starting model (blue) residuals and tomographic model (brown) residuals.

The figures below, figures 23 – 27, show the residuals of the dense receiver region.

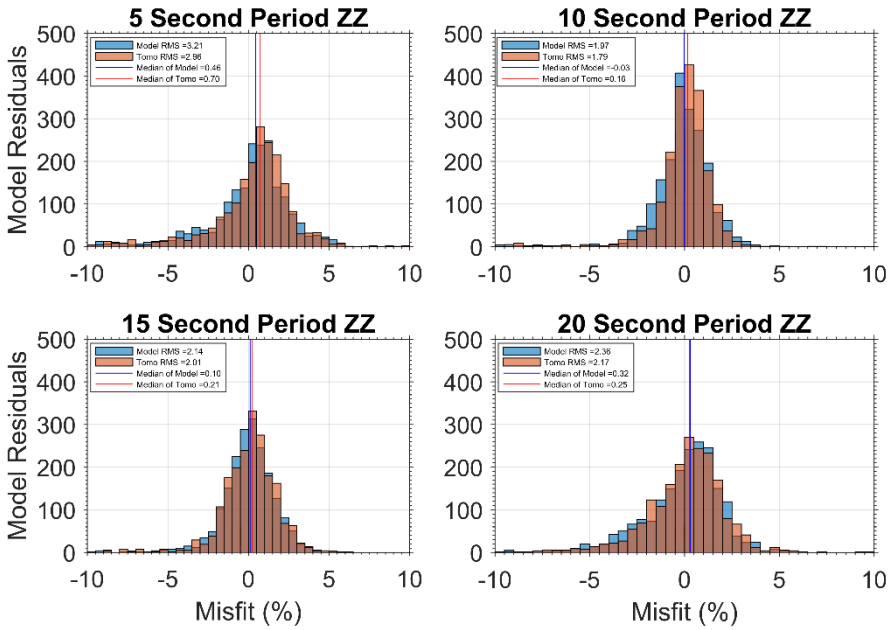

Figure 23: Histograms showing starting model (blue) residuals and tomographic model (brown) residuals for the dense receiver region.

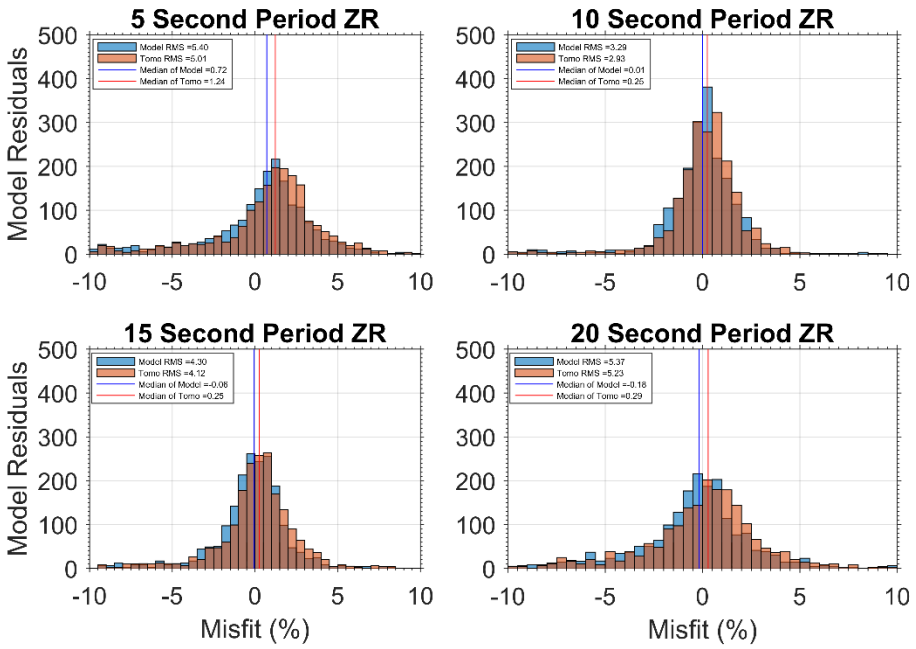

Figure 24: Histograms showing starting model (blue) residuals and tomographic model (brown) residuals for the dense receiver region.

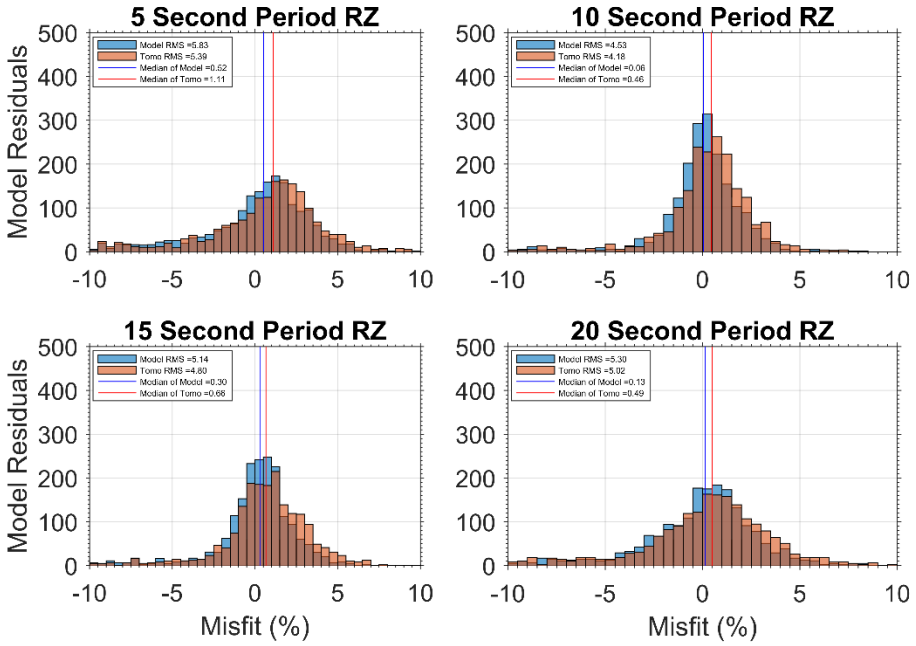

Figure 25: Histograms showing starting model (blue) residuals and tomographic model (brown) residuals for the dense receiver region.

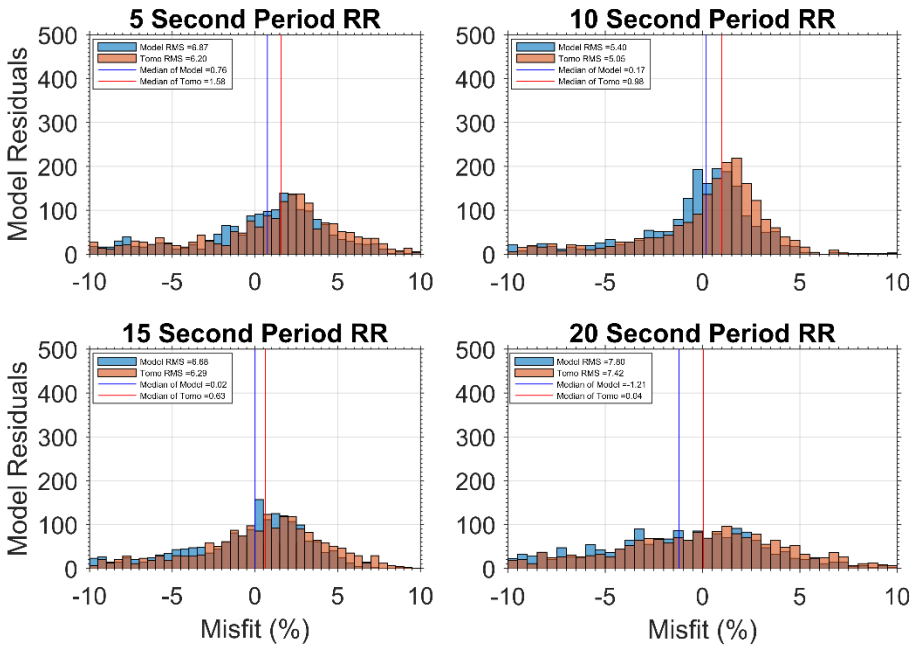

Figure 26: Histograms showing starting model (blue) residuals and tomographic model (brown) residuals for the dense receiver region.

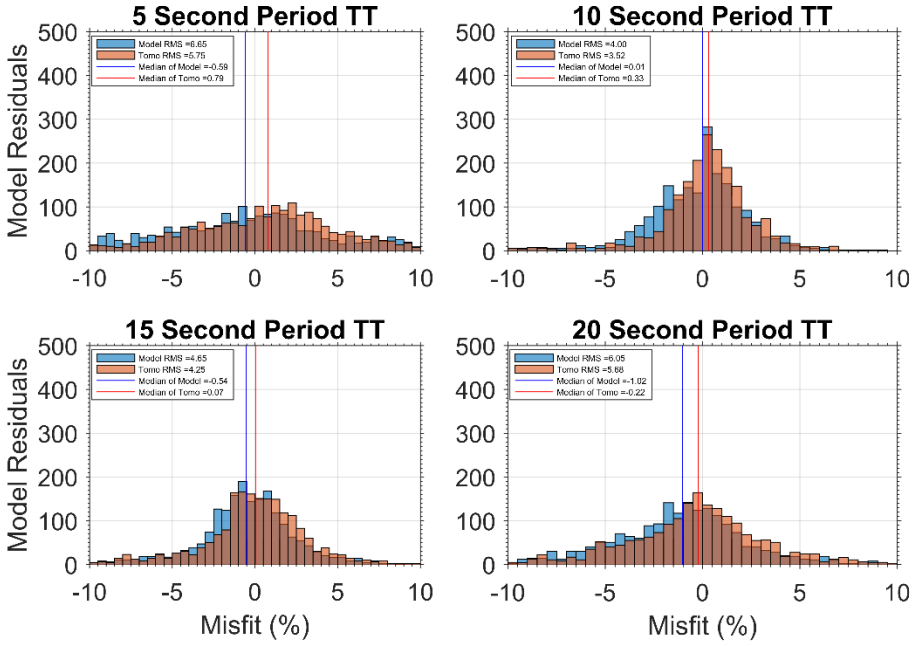

Figure 27: Histograms showing starting model (blue) residuals and tomographic model (brown) residuals for the dense receiver region.

5.4. Vs at Depth:

Surface wave maps based on period are useful in visualizing velocities across the state but are not easily useful for any further academic or professional use. Converting periods to depths provides a velocity model of various layers at depth, which is more intuitive and easily understandable. The basic method of inversion is similar to the dispersion measurements and subsequent tomographic inversion. The difference here is that there are now velocity estimations for each period on a grid across the state. Each grid point has a different velocity based upon the period. This now acts as a dispersion measurement at that location and those velocities are inverted to depth in the form of Vs velocities. Below are the figures showing the Vs velocities in the state at each depth.

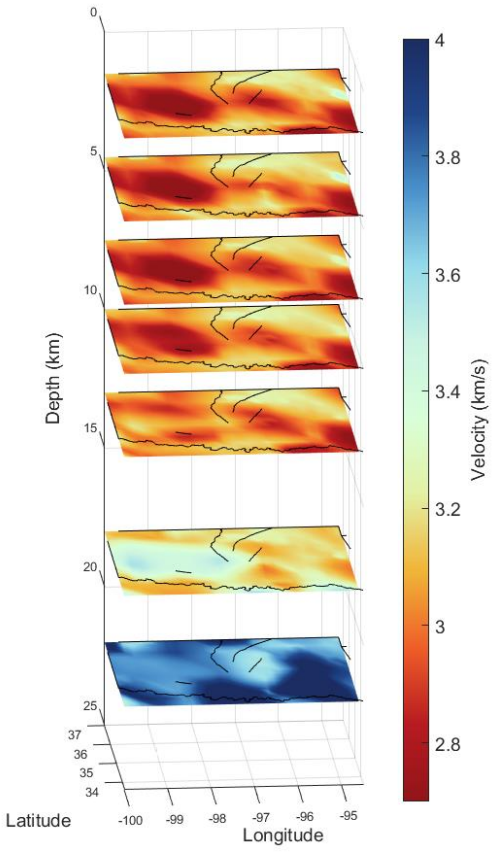

Figure 28: Showing 3-dimensional image of each velocity layer in the model. Layers from surface down are at a depth of 1 km, 5 km, 8 km, 10 km, 13 km, 18 km, and 22 km respectively. Velocity is portrayed by absolute velocity on a color scale to show the change from layer to layer.

The top few layers in figure 28 seem to be relatively similar to each other, but velocity begins to drastically increase between 13 and 18 km depths. Due to the great difference in velocity from the topmost layer to deepest layer, smaller scale structure is hard to visualize with the extent of the color bar. Figure 28 only shows the relative change between the layers. The figures following show each layer individually, with a modified color scale, and the structure can be identified much more easily.

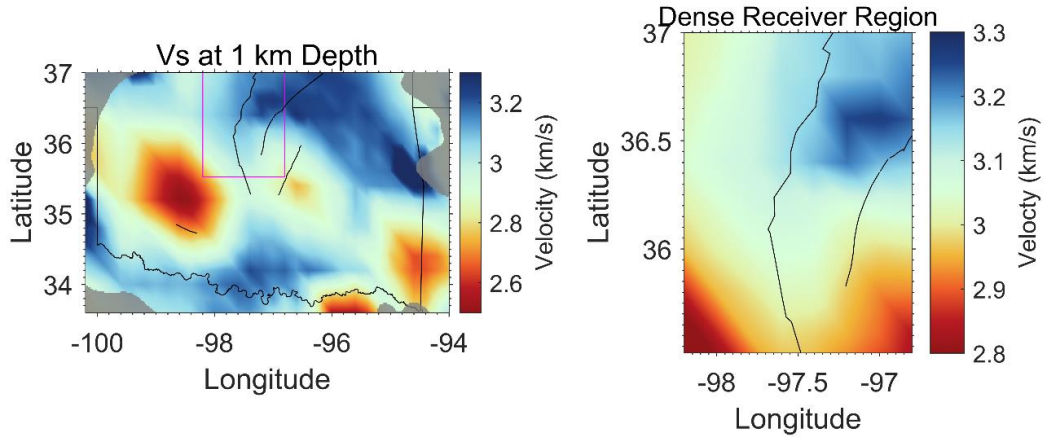

Figure 29: All the images here are for the layer at 1 km depth. Left image shows the velocity in km/s across the inversion area. The right image is a zoomed-in portion of the state showing the velocity of the region with high station density. Gray overlay on left shows region of unreliable tomographic results.

For the layer at 1 km depth, the velocity generally ranges between 2.4 km/s and 3.4 km/s. Figures 30 – 35 are similar to figure 29 above. They each show fast and slow velocity in various regions of the state due to changing geology. In general, some fast velocity structures can be seen to the northeast and the south. There are also two regions of low velocity. The slowest region is in the southwest corner of the state, while the next one is just to the east.

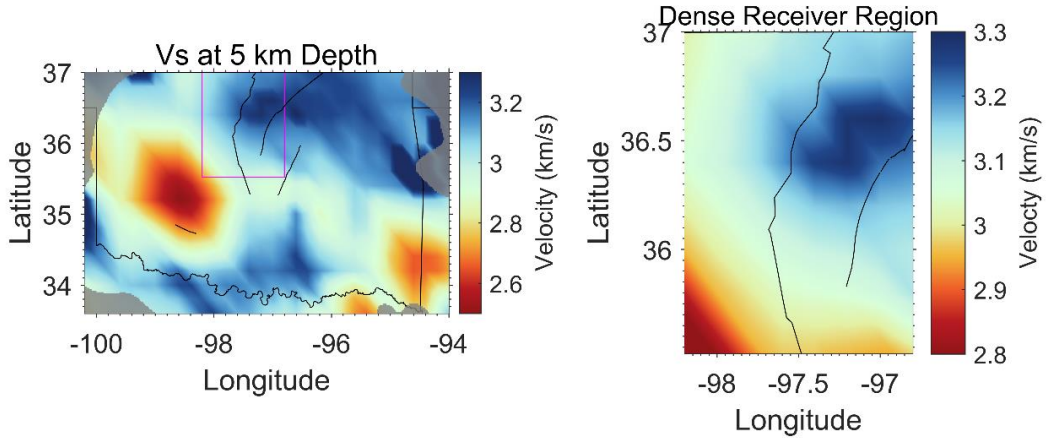

Figure 30: Same as figure 29 but at depth of 5 km.

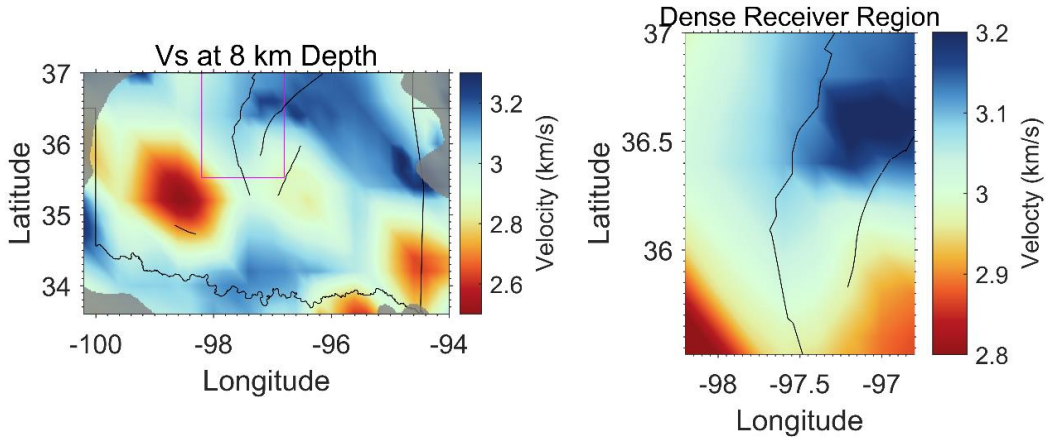

Figure 31: Same as figure 29 but at depth of 8 km.

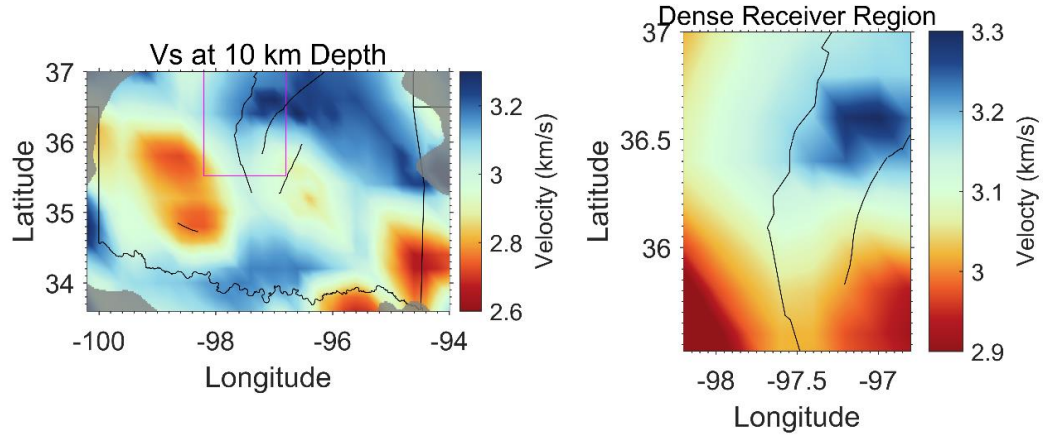

Figure 32: Same as figure 29 but at depth of 10 km.

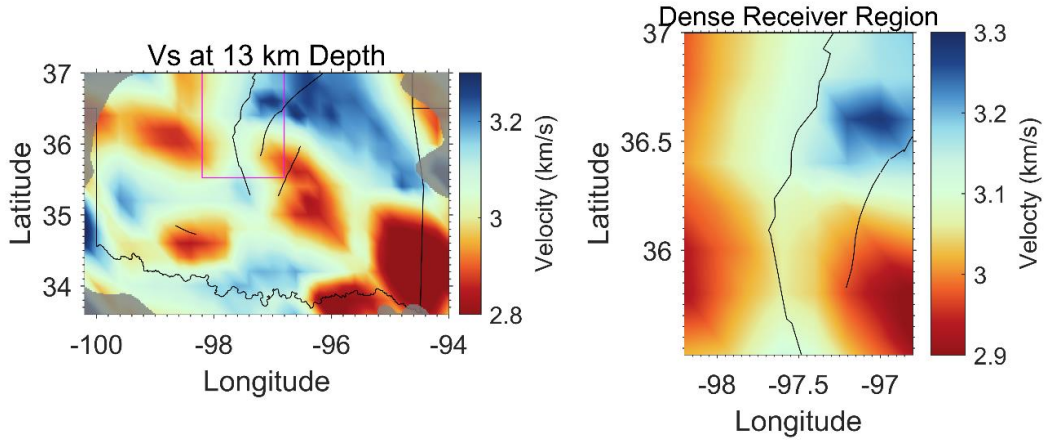

Figure 33: Same as figure 29 but at depth of 13 km.

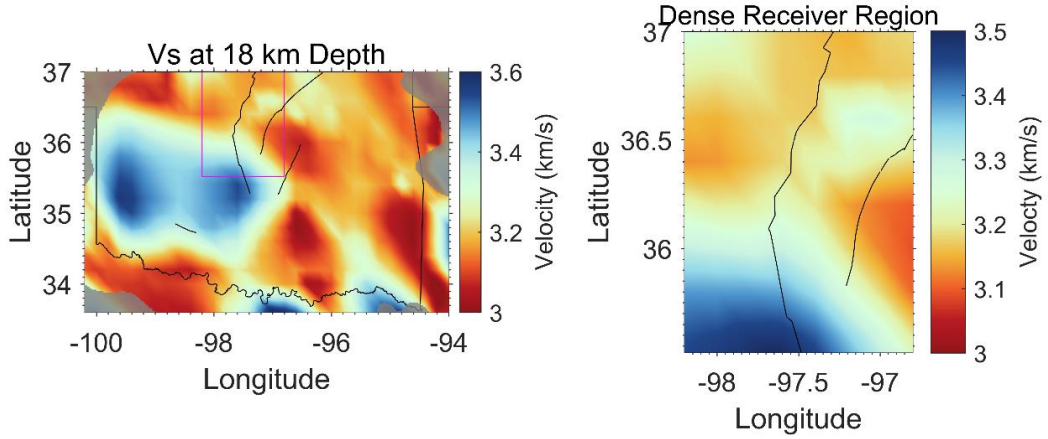

Figure 34: Same as figure 29 but at depth of 18 km.

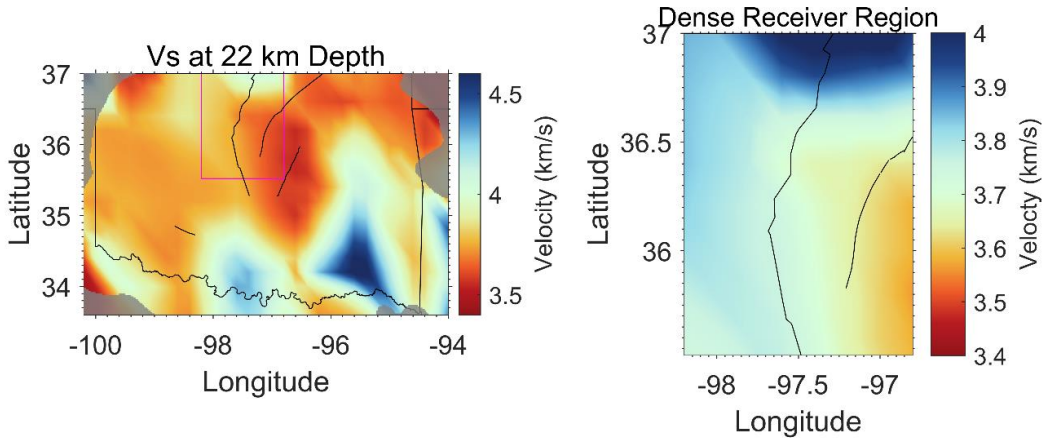

Figure 35: Same as figure 29 but at depth of 22 km.

The model as it has been shown above is a 3D approximation of seismic velocity. Each figure above provides velocity estimations at a given depth across the state. It can also be helpful to visualize velocity as depth changes. The figures below show velocity changing at depth across either a line of latitude or longitude. Figure 36 shows the locations of each cross-section and figures 37-38 are the respective cross-sections.

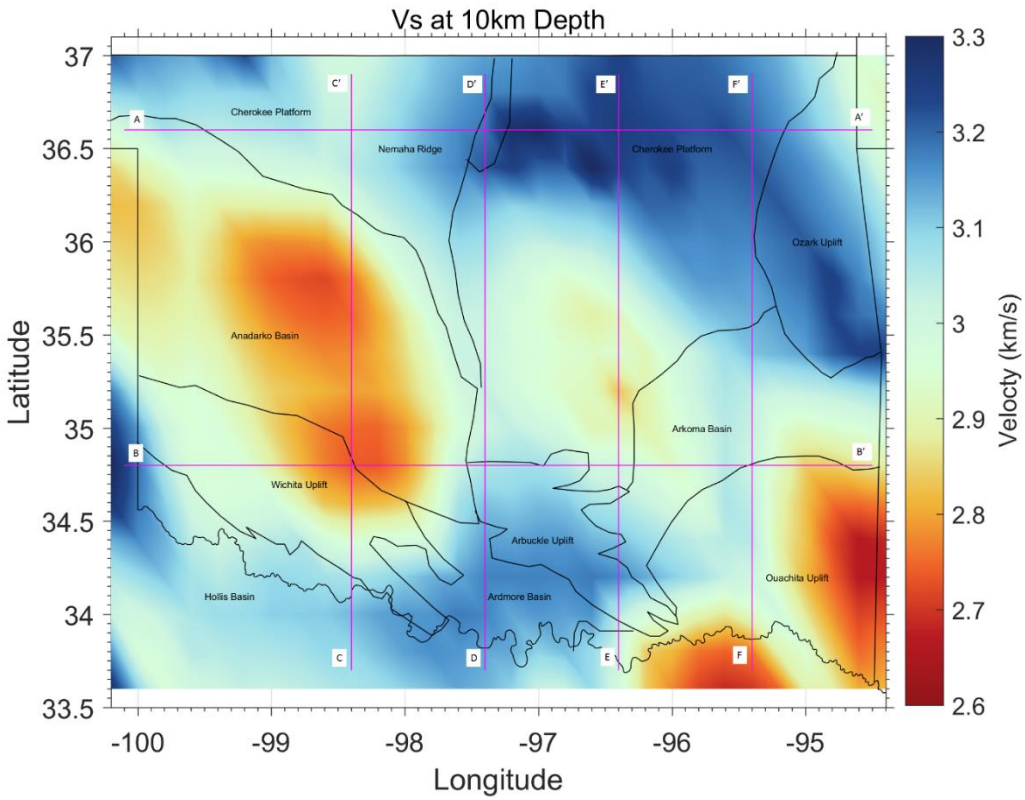

Figure 36: Each purple line helps to show the location of each cross-section in the figures below. Latitude lines are at 36.6 and 34.8 degrees. Longitude lines are at -95.4, -96.4, -97.4, and -98.4 degrees. Black outlines show the boundaries of the geologic provinces (Modified from Johnson, 2008).

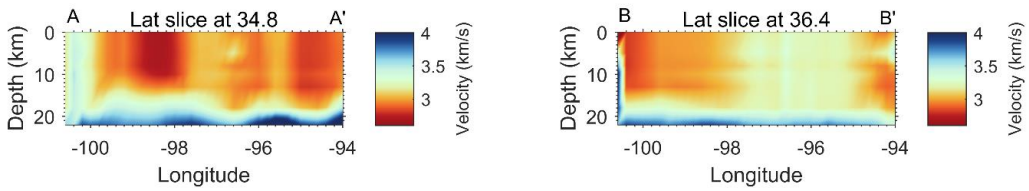

Figure 37: Cross-Section of velocities at Latitude of 34.8 and 36.4 degrees.

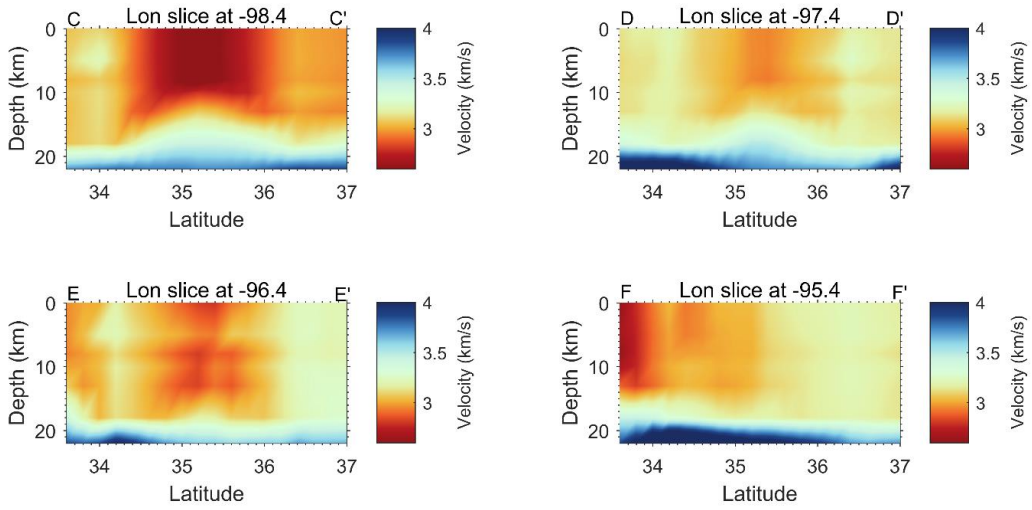

Figure 38: Cross-Section of velocities at Longitude of -98.4, -97.4, -96.4, and -95.4 degrees.

Chapter 6: Discussion

Any model will have limitations and those should be addressed for complete understanding. One limitation to this model is that the initial tomographic inversion was done using an unrealistic starting model for velocity. The starting model was a uniform velocity value of 3 km/s across the entire region, which is not representative of the varying geology across the state or at depth. One way to improve the model would be to use a more geologically realistic velocity model for the starting model of another inversion. Additionally, the histograms above do not show significant model improvement, but do show some model improvement. The ideal histogram would be a spike in the middle showing that 100% of model residuals have no difference between the observed travel-times. There is no perfect model and therefore the ideal histogram is not possible to attain. However, the taller and narrower the bars are will indicate greater model accuracy to true values.

One advantage to this model is that it is on a nearly state-wide level with excellent station coverage. There are stations located in all directions surrounding the state and are relatively equally spaced (2009 – 2012). This station configuration allows for a constant coverage of the state that will increase resolution due to many crossing ray-paths. In addition to those stations there are many stations that have been placed in a densely packed region in the northern part of the state. This higher station density increases the model resolution in that area. Currently the model is able to resolve velocity every 25 km in the dense station coverage and approximately 50 km outside of that. Figure 39 below

shows the resolution of the tomographic model. As stated above, the dense receiver region has a much higher resolution than that of the rest of the state.

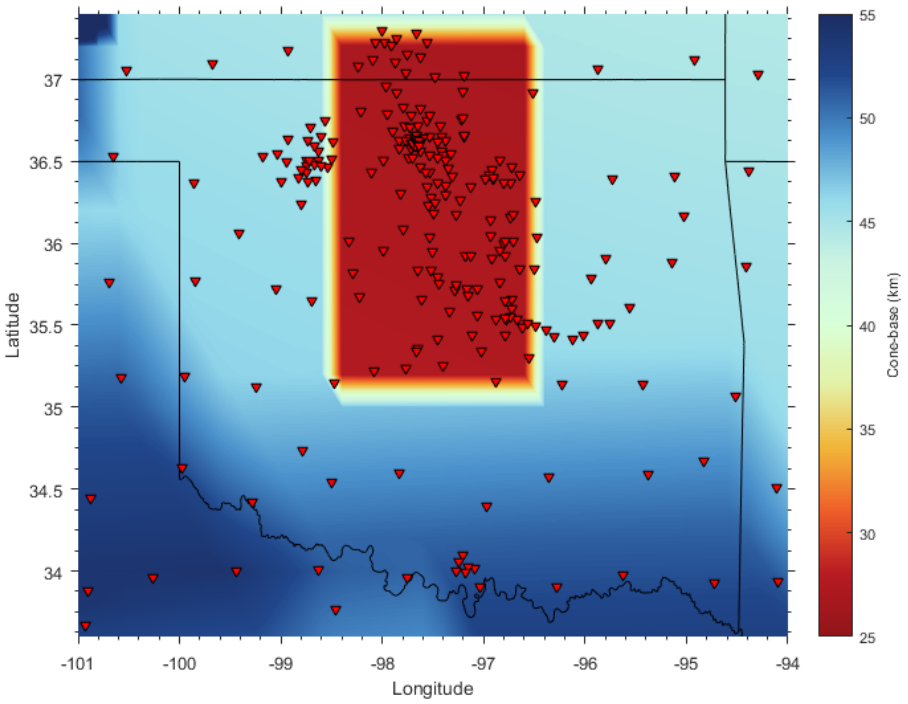

Figure 39: Shows the gaussian cone base of the tomographic model at each point. It is representative of the resolution of the model. Dense receiver region resolves at about 25 km, while the north part of the state is generally around 45 km and southern Oklahoma is resolved to about 50 km.

Seismic velocity is dependent upon geologic lithology, structure, and conditions (temperature, confining stress, and geologic history). It is therefore also important to understand what geologic features are represented within the velocity model. Figure 40 below outlines the geologic provinces of Oklahoma and gives a good summary of the different major structures that are present today. Most notably are the Anadarko Basin, Wichita Uplift, Arbuckle Uplift, Ouachita Uplift, and the Nemaha Uplift/Ridge.

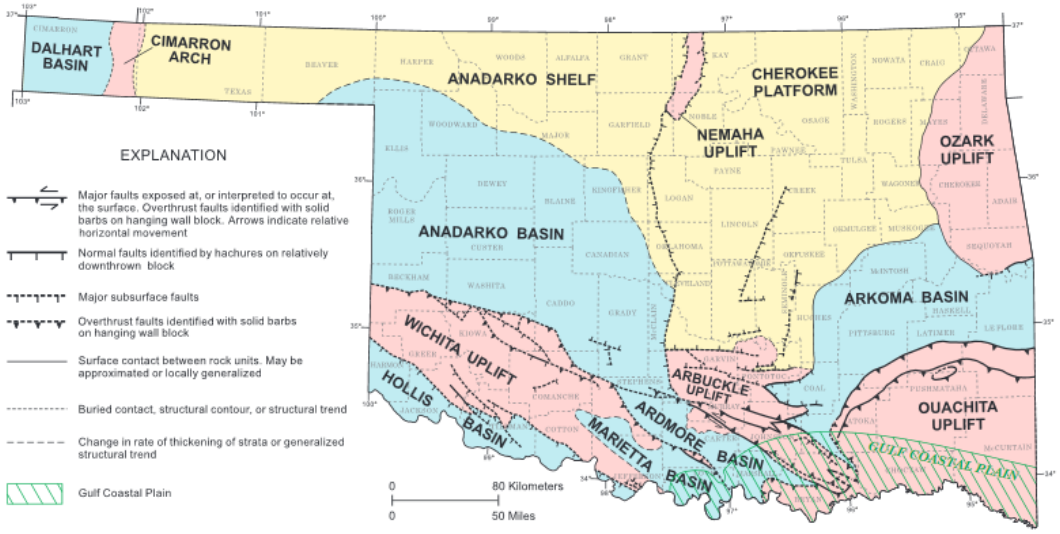

Figure 40: Showing major structure within Oklahoma. Pink color denotes regions of uplift, blue shows basin boundaries, and yellow show location of the shelf/platform. See appendix figure A9 for cross sections of geologic provinces. (Johnson 2008).

Based on the model discussed above in figures 29-35, and comparing it with Figure 40, it is likely that the sedimentary Anadarko Basin is responsible for the slower velocity region in the west central part of the state as opposed to igneous rocks elsewhere. The Anadarko Basin is the largest and most extensive basin in Oklahoma, and with the thickest sediment in the US. As a result, we expect to see a slower velocity for this region in the velocity models. This slower velocity is around 2.5 km/s in the west central part of the state at 1 km, 5 km, 8 km, and 10 km depths. The slow velocity remains present up to the 10 km depth where we see the velocity begin to increase to approximately 2.8 km/s, though the Anadarko Basin reaches as deep as 15 km (Keller 2014).

The faster velocities to the southwest of the Anadarko Basin along the state border and the faster velocity just to the southeast of the basin can be linked to the Wichita Mountain Uplift and the Arbuckle Mountain Uplift. The Wichita Mountains have no major sedimentary layers to slow velocity. Instead the igneous and metamorphic Cambrian

rocks are found near the surface. Additionally, the Arbuckle Mountains have very shallow Precambrian basement but with small sedimentary layers near the surface (Johnson 2008). These uplifts are likely the cause of the faster velocities to the southwest and southeast of the Anadarko Basin.

The slow velocity region in the central part of the state directly to the east of the Anadarko Basin has no apparent geologic feature which explains the slow anomaly. It is too far west to be the Arkoma Basin and too far east to be attached to the Anadarko Basin. In Ratre (2016) that region is shown to have a negative magnetic anomaly, figure A10, which is not expected to occur, and no reason is given for this apparent unrealistic anomaly. In summary, there is no currently known geologic feature in the region to explain this low velocity zone.

The slower velocity found in the southeast corner from 1-13 km depths is likely due to the Ouachita Uplift and Arkoma Basin. The Ouachita Uplift and Arkoma Basin are largely made up of Pennsylvanian, Mississippian, Devonian, Silurian, Ordovician, and Cambrian sedimentary rocks. The sedimentary rocks which make up the Ouachita Mountains and the Arkoma Basin can be found as deep as 9 km depth (Johnson 2008). These depths seem consistent with the velocity models shown above, except we see the slow velocity penetrating as deep as 13 km. This may be due to the Cambrian igneous and metamorphic rocks in the Arkoma basin, which are vertically below the sedimentary rocks but still a part of the basin and above the Precambrian basement which would be faster still.

Another trend in the velocity model is that the northeast typically has faster velocities than that of the rest of the state. This can be explained by the reduced depth of the Precambrian basement. Figure 41, modified from Crain et al. (2018), shows the elevation contours of the Precambrian basement in most of Oklahoma.

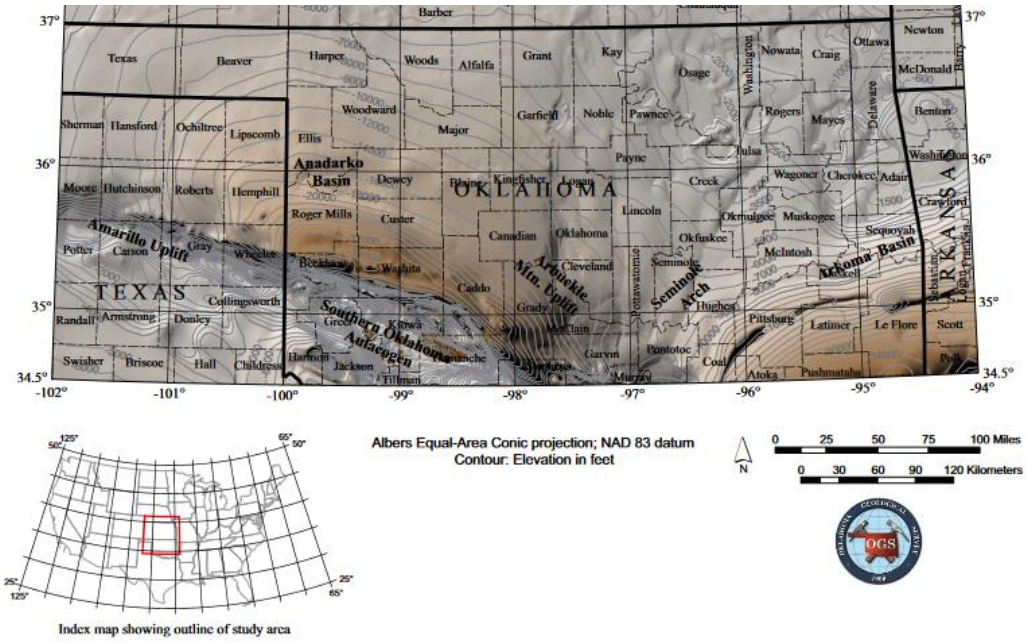

Figure 41: Elevation contours of Precambrian basement in Oklahoma. Note that contour units are in feet. Modified from Crain et al. (2018).

The northeast part of Oklahoma, as shown by figure 41, has the Precambrian basement as shallow as 300 m depth, which can be attributed to thinning of sedimentary structure in the Cherokee Platform to the northeast and to the uplift of Precambrian granitic structure from the Ozark Uplift. The 300 m depth of the Precambrian basement explains why even at a depth of 1.5 km, along the Cherokee Platform, the velocities are faster when compared with the rest of the state. It is because the Precambrian basement is older, granitic rock which is seismically much faster than that of younger, sedimentary rock. In

the southeast, igneous basement is found as deep as 10 km and in the southwest as deep as 20 km. It is also important to note that basement structure in Oklahoma is not simple, uniform, and with a constant, gradual slope. There are some complicated basement structures in the central-east and in the southwest. These heterogeneities play a part in the velocity structure of the state below 13 km depths.

In the very northeast corner of the state, from approximately 36.5 to 37.0 degrees of latitude and -94.8 to -94.6 degrees longitude, there is a small region where the velocity is slower (2.9-3.1 km/s) than that of the fast, granitic basement (3.1-3.4 km/s) in northeastern Oklahoma. This coincides with a region of economic mineral exploration, with a known history of hydrothermal alteration (McKnight et al. 1970). This hydrothermal alteration may be the cause of slower velocities due to that region containing fractured, warmer, altered granitic rock.

Another feature of note is the Nemaha Uplift, which extends from the north central part of the state into central Oklahoma. It has significant vertical throw that puts basement to the east at shallower levels than sedimentary layers to the west (McBee Jr. 2003). In the velocity models, a quick shift in fast to slow velocity in north-central Oklahoma is likely due to the Nemaha Ridge. The east side of the Nemaha Ridge has been up-thrown and faster granitic basement is nearer to the surface than the west, which has sedimentary layers closer to the surface. This change from fast to slow velocity, from east to west, is seen as deep as 13 km, but does become less pronounced as depth increases.

Lastly, at 18 km depth we see a sharp increase in velocity as well as the structural features from basins and uplifts disappearing. At these depths we are seeing deep basement structure. As depth increases below basin and uplift structure, we expect to see velocity become more homogeneous throughout the state. This is exactly what we see in the 18 km and 22 km depth slices. The faster velocity region in southeast Oklahoma, in the 22 km depth may be due to a mantle intrusion into the crustal igneous basement from a continental rift boundary, figure A11 (Ratre 2018, Whitmeyer et al. 2007).

Chapter 7: Conclusion

Understanding the velocity structure in the state of Oklahoma is extremely important. Oklahoma has been very active in seismicity in recent years and there is an abundance of research being performed. Earthquake location is often the first step in many areas of research. Locating an earthquake requires previous knowledge of seismic wave travel-times. Seismic waves are observed and relative travel-times between stations give an idea of approximately where an earthquake originated. However, most often the first arrival of a seismic waves travel along a curved path at depth before being recorded at the surface. Therefore, using this velocity model can help to constrain the location of the earthquakes more accurately by providing velocity estimations along any path in the state.

Not only does understanding velocities improve our ability to locate earthquakes more accurately, it also reveals the tectonic history of Oklahoma. Shallow granitic basement can be observed in the northeast due to faster velocities, while the basins are characterized by slower velocities. The tomographic model confirms known geology, while providing new information about the velocity of those tectonic regions.

In the study performed by Ekstrom (2014), Love and Rayleigh wave phase velocity maps were created using short period noise correlation. The study spanned most of the continental United States and includes the state of Oklahoma. Both Love and Rayleigh wave velocities in Ekstrom (2014), in Oklahoma, appear to be slower in the southwest and southeast, while being faster in the northeast. This agrees with the velocity model

presented here, however the resolution is improved in this study due to the inclusion of local broadband stations.

Ultimately no model is perfect, and this model is no exception. As time progresses, new techniques are created to develop and improve models. The most beneficial change to make is to install more stations at higher densities throughout the state to increase station coverage. Resolution is dependent upon inversion parameters but is even more dependent upon station coverage. Therefore, incorporating new stations in new locations throughout the state of Oklahoma is one of the best ways to increase the resolution of velocities. It is ultimately the hope that this velocity model will prove useful and reliable for the continuing research into seismicity in Oklahoma.

References

Aki, K., 1957, Space and time spectra of stationary stochastic waves, with special reference to microtremors, Bulletin of Earthquake Research Institute 25, 415-457.

Barmin, M.P., Ritzwoller, M.H., Levshin, A.L., 2001. A Fast and Reliable Method for Surface Wave Tomography. Pure and Applied Geophysics 158, 1351-1375.

Bensen, G.D., Ritzwoller, M.H., Barmin, M.P., Levshin, A.L., Lin, F., Moschetti, M.P., Shapiro, N.M., Yang, Y., 2007. Processing seismic ambient noise data to obtain reliable broad-band surface wave dispersion measurements. Geophys. J. Int. (2007) 169, 1239-1260.

Claerbout, J.F., 1968. Synthesis of a layered medium from its acoustic transmission response. Geophysics 33. 264-269.

Crain, K.D., Chang, J.C., 2018, Elevation of Precambrian Basement. Oklahoma Geological Survey Open-File Report 1-2018.

Curtis, A., Gerstoft, P., Sato, H., Snieder, R., Wapenaar, K., 2006. Seismic interferometry – turning noise into signal. The Leading Edge September 2006, 1082-1092.

Draganov, D., Ruigrok, E., 2015. Passive Seismic Interferometry for Subsurface Imaging. Encyclopedia of Earthquake Engineering. DOI 10.1007/978-3-642-36197-5_378-1.

Ekstrom, G., 2014, Love and Rayleigh phase-velocity maps, 5-40 s, of the western and central USA from USArray data. Earth and Planetary Science Letters 402, 42-49.

Herrmann, R. B. (2013) Computer programs in seismology: An evolving tool for instruction and research, Seism. Res. Lettr. 84, 1081-1088, doi:10.1785/0220110096.

Hincks, T., Aspinall, W., Cooke, R., Gernon, T., 2018. Oklahoma's induced seismicity strongly linked to wastewater injection depth. Science, DOI: 10.1126/science.aap7911.

Johnson, K.S., 2008. Geologic History of Oklahoma. Oklahoma Geological Survey Educational Publication 9.

Keilis-Borok, V.I., Levshin, A.L., Yanovskaya, T.B., Lander, A.V., Bukchin, B.G., Barmin, M.P., Ratnikova, L.I., Its, E.N., 1989. Seismic Surface Waves in Laterally Inhomogeneous Earth. Modern Approaches in Geophysics Vol 9.

Keller, G.R., 2014, The Southern Oklahoma Aulacogen: It's a classic. In Suneson, N., 2014, Igneous and Tectonic History of the Southern Oklahoma Aulacogen. Oklahoma Geological Survey Guidebook 38, 389-391.

Keranen, K.M., Weingarten, M., 2018, Induced Seismicity. Annual Review of Earth and Planetary Sciences 2018.46:149-174.

Levshin, A.L., Yanovskaya, T.B., Lander, A.V., Bukchin, B.G., Barmin, M.P., Ratnikova, L.I., Its, E.N., 1989. Seismic Surface Waves in a Laterally Inhomogeneous Earth, ed. Keilis-Borok, V.I., Kluwer, Norwell, Mass.

Lin, F., Moschetti, M.P., Ritzwoller, M.H., 2008, Surface wave tomography of the western United States from ambient seismic noise: Rayleigh and Love wave phase velocity maps. Geophysics. J. Int. 173, 281-298.

Lin, F., Ritzwoller, M.H., Snieder, R., 2009. Eikonal tomography: surface wave tomography by phase front tracking across a regional broad-band seismic array. Geophy. J. Int. (2009) 177, 1091-1110.

Luza, K.V., Madole, R.F., Crone, A.J., 1987, Investigation of the Meers Fault, Southwestern Oklahoma. Oklahoma Geological Survey Special Publication 87-1.

Marsh, S.J., Holland, A.A, 2016, Comprehensive Fault Database and Interpretive Fault Map of Oklahoma. Oklahoma Geological Survey Open-File Report 2-2016.

McBee Jr., W., 2003, Nemaha Strick-Slip Fault Zone, Search and Discovery Article #10055, Adapted from oral presentation at AAPG Mid-Continent Section Meeting, October 2003.

McKnight, E. T., Fischer, R. P., 1970, Geology and Ore Deposits of the Picher Field Oklahoma and Kansas. United States Geological Survey Professional Paper 588.

Mordret, A., Landes, M., Shapiro, N. M., Singh, S.C., Roux, P., Barkved, O. I., 2013, Near-surface study at the Valhall oil field from ambient noise surface wave tomography. Geophys. J. Int. 193, 1627-1643.

Nakata, N., Chang, J.P., Lawrence, J.F., Boue, P., 2015, Body Wave extraction and tomography at Long Beach, California, with ambient-noise interferometry. J. Geophys. Res. Solid Earth, 120, 1159-1173, doi: 10.1002/2015JB011870.

Nicolson, H., Curtis, A., Baptie, B., Galetti, E., 2012. Seismic interferometry and ambient noise tomography in the British Isles. Proceedings of the Geologists Association 123. 74-86.

Nishida, K., Kawakatsu, H., Obara, K., 2008, Three-dimensional crustal S wave velocity structure in Japan using microseismic data recorded by Hi-net tiltmeters. Journal of Geophysical Research, vol 113, B10302.

Perry Jr., W.J., 1989, Tectonic Evolution of the Anadarko Basin Region, Oklahoma. United States Geologic Survey Bulletin 1866-A.

Poli, P., Pedersen, H. A., Campillo, M., and the POLENET/LAPNET Working Group, 2012, Emergence of body waves from cross-correlation of short period seismic noise. Geophys. J. Int. 188, 549-558.

Ratre, P., 2016, Integrated Geophysical Study for Subsurface Characterization of Basement in the Cherokee Platform, Northeastern Oklahoma. The University of Tulsa, Graduate School, M.S. Thesis.

Ratre, P., 2018, Personal Correspondence, University of Oklahoma.

Rawlinson, N., Fichtner, A., Sambridge, M., Young, M.K., 2014. Seismic Tomography and the Assessment of Uncertainty. Advances in Geophysics, vol 55.

Ritima Das and S S Rai 2016 J. Phys.: Conf. Ser. 759 012006.

Shapiro, N.M., Campillo, M., Stehly, L., Ritzwoller, M.H., 2005, High-Resolution Surface-Wave Tomography from Ambient Seismic Noise. Science 29, 1615-1617.

Snieder, R., 2004. Extracting the Green's function from the correlation of coda waves: A derivation based on stationary phase. Physical Review E69 046610.

Wapenaar, Kees, Draganov, Deyan, Snieder, Roel, Campman, Xander, Verdel, Arie, 2010. Tutorial on seismic interferometry: Part 1 – Basic principles and applications., Geophysics. Vol. 75, No. 5.

Whitmeyer, S.J., Karlstrom, K.E., 2007, Tectonic model for the Proterozoic growth of North America. Geosphere v. 3 no. 4, 220-259.

Zhao, Y., 2013. Passive seismic interferometry in the real world: Application with microseismic and traffic noise. Dissertation for degree of Doctor of Philosophy, University of California, Berkely.

Zhu, H., 2018. Crustal wave speed structure of North Texas and Oklahoma based on ambient noise cross-correlation functions and adjoint tomography. Geophysical Journal International vol 214, issue 1, 716-730.

Zigone, D., Ben-Zion, Y., Campillo, M., Roux, P., 2015. Seismic Tomography of the Southern California Plate Boundary Region from Noise-Based Rayleigh and Love Waves. DOI 10.1007/s00024-014-0872-1.

Appendix

Station Coverage/Earthquakes

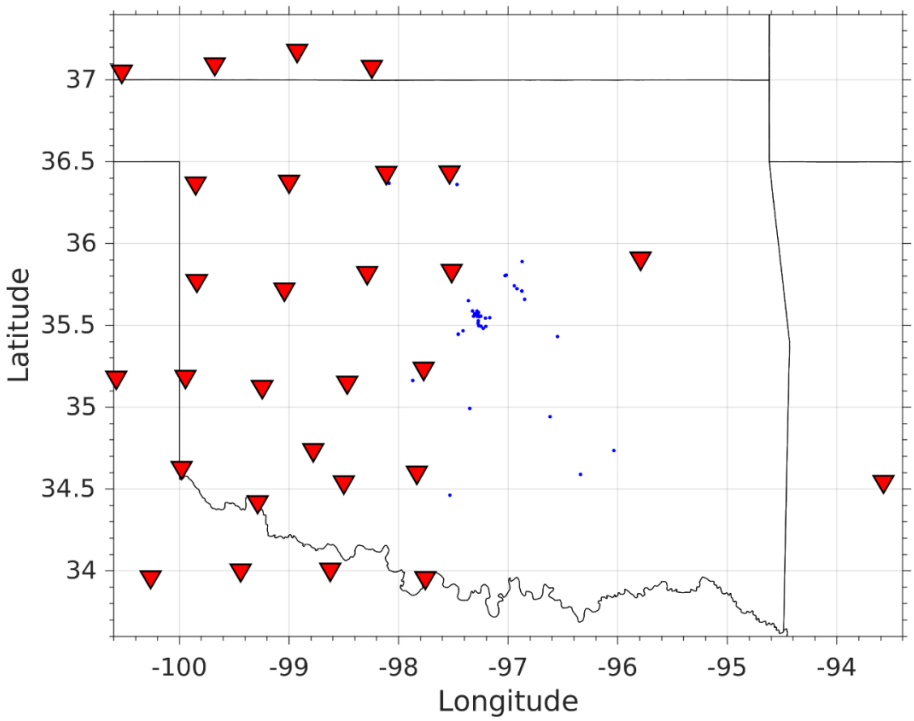

Figure A1: Station coverage and earthquakes, 2009.

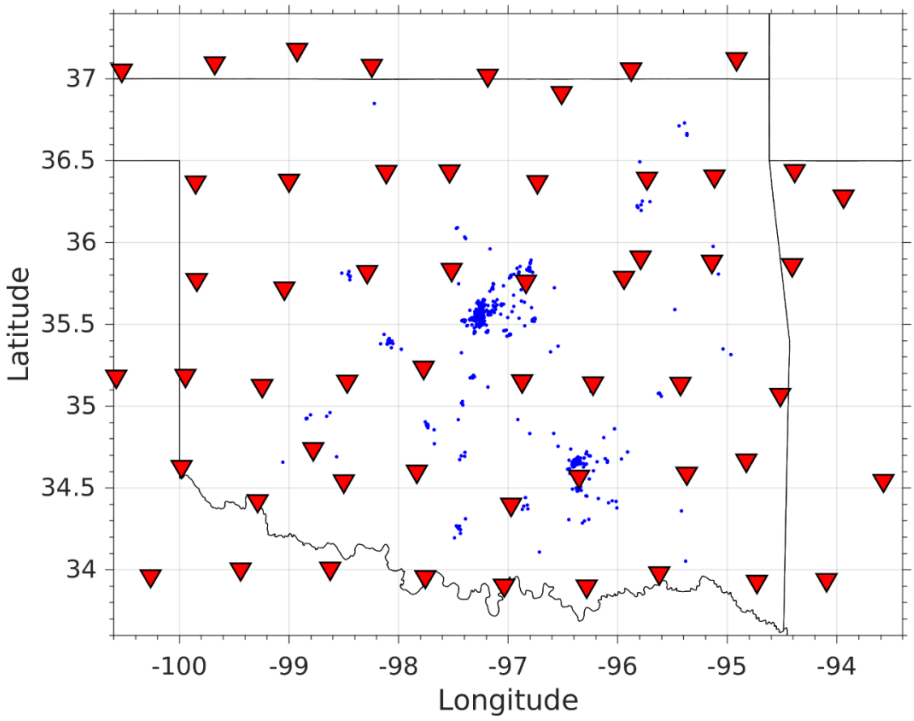

Figure A2: Station coverage and earthquakes 2010.

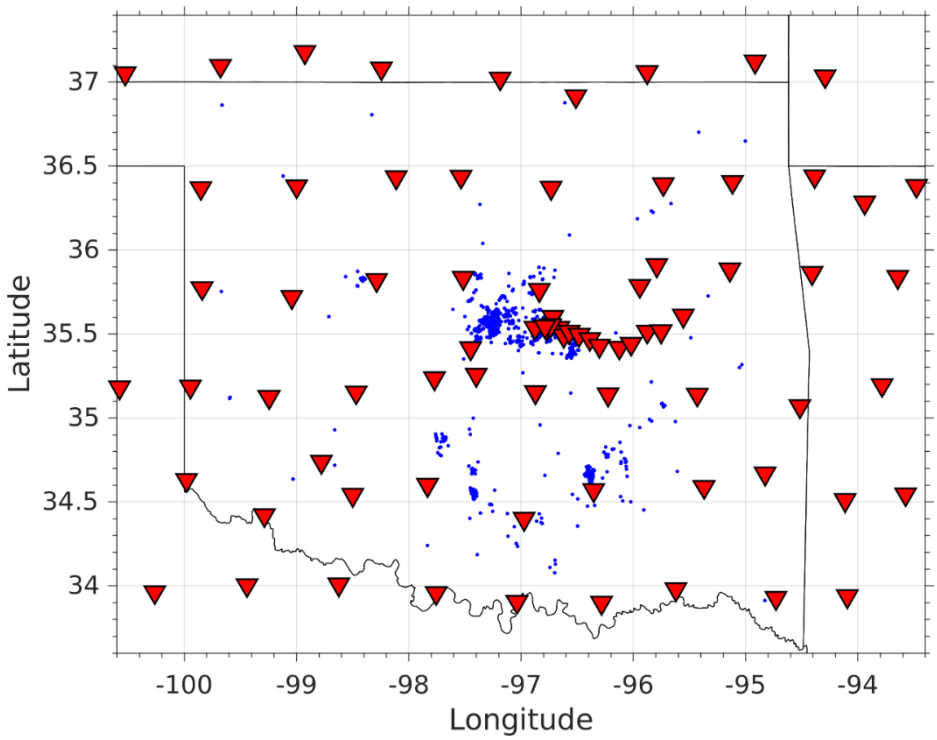

Figure A3: Station coverage and earthquakes 2011.

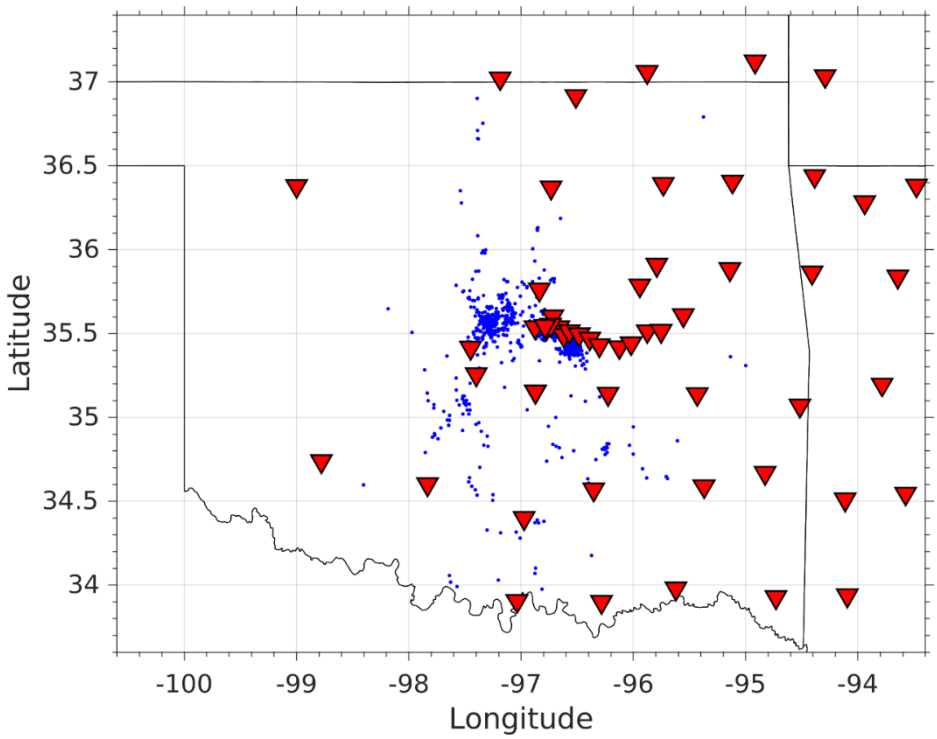

Figure A4: Station coverage and earthquakes 2012.

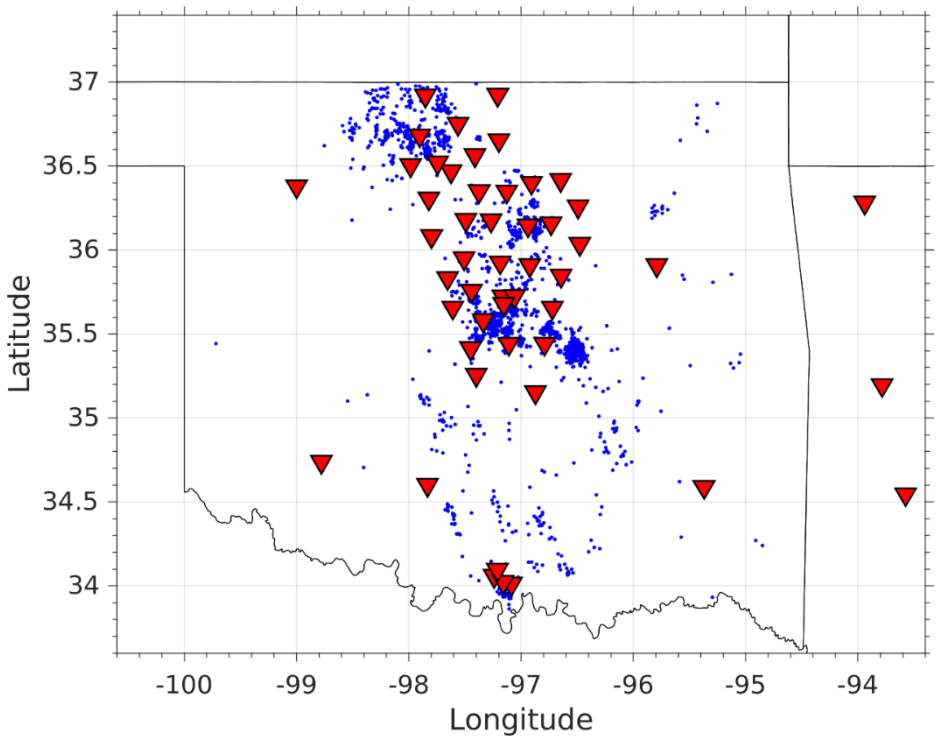

Figure A5: Station coverage and earthquakes 2013.

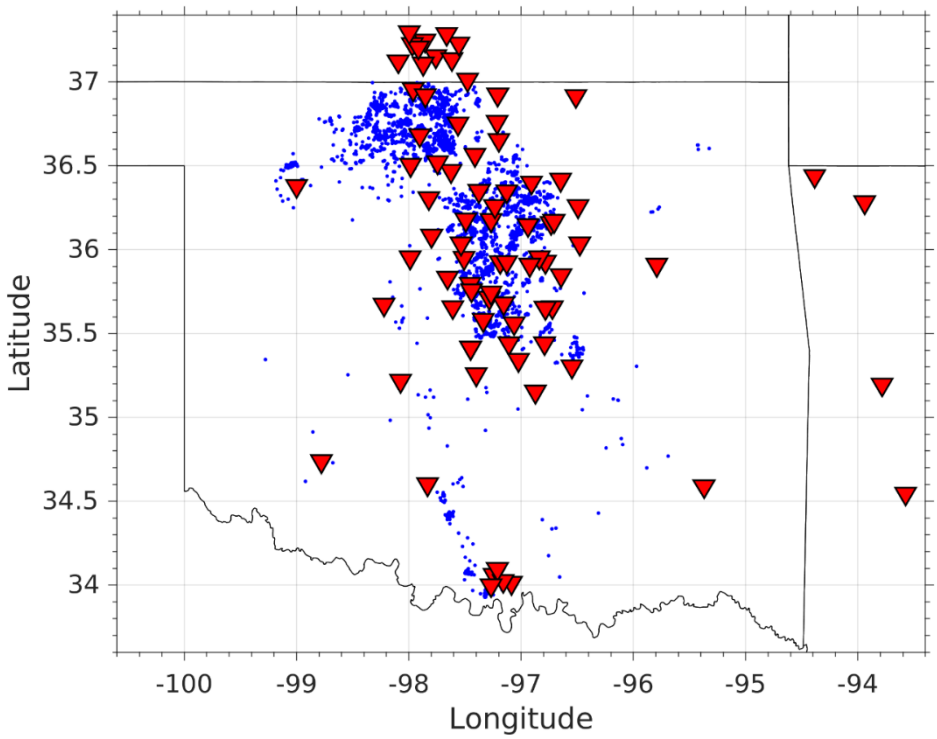

Figure A6: Station coverage and earthquakes 2014.

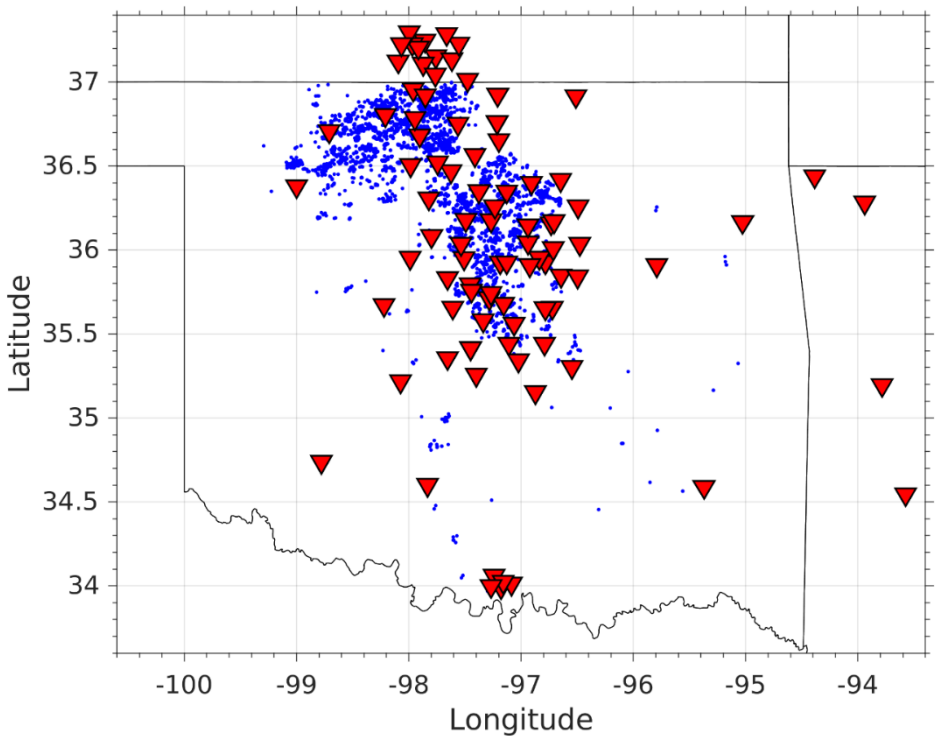

Figure A7: Station coverage and earthquakes 2015.

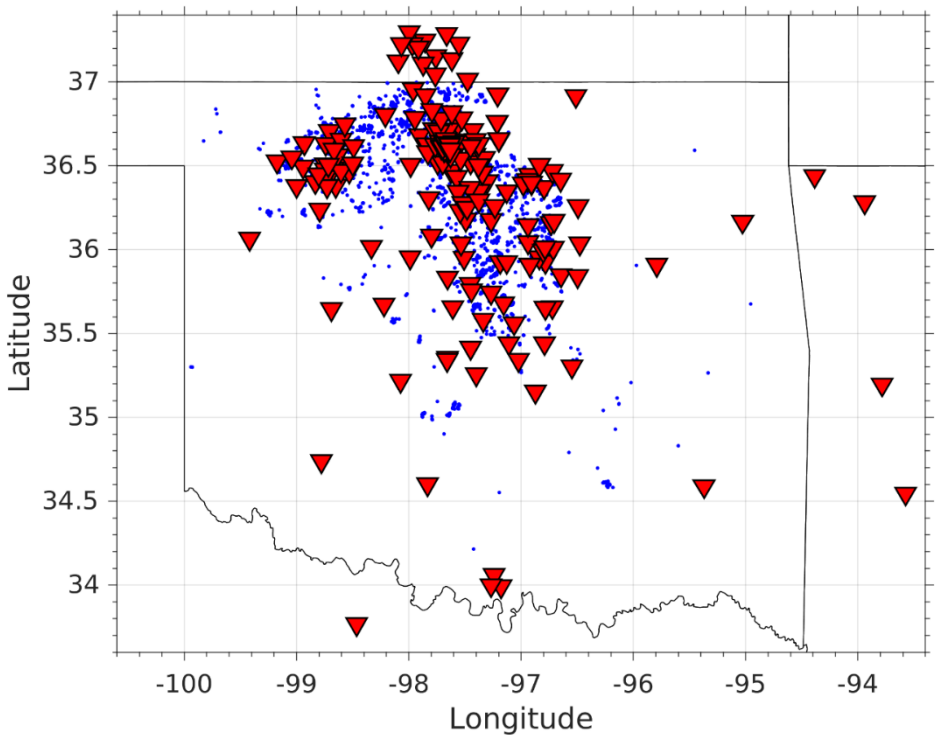

Figure A8: Station coverage and earthquakes 2016.

Cross-Sections of Geologic Provinces

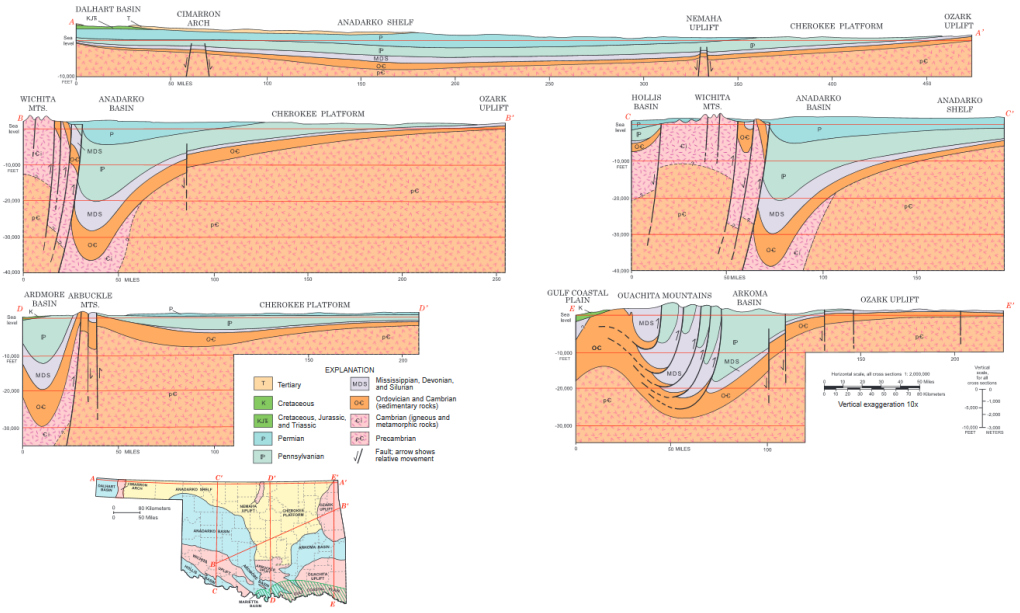

Figure A9: Cross-Sections of Geologic Provinces. A-A', B-B', C-C', D-D', E-E'. Johnson (2008).

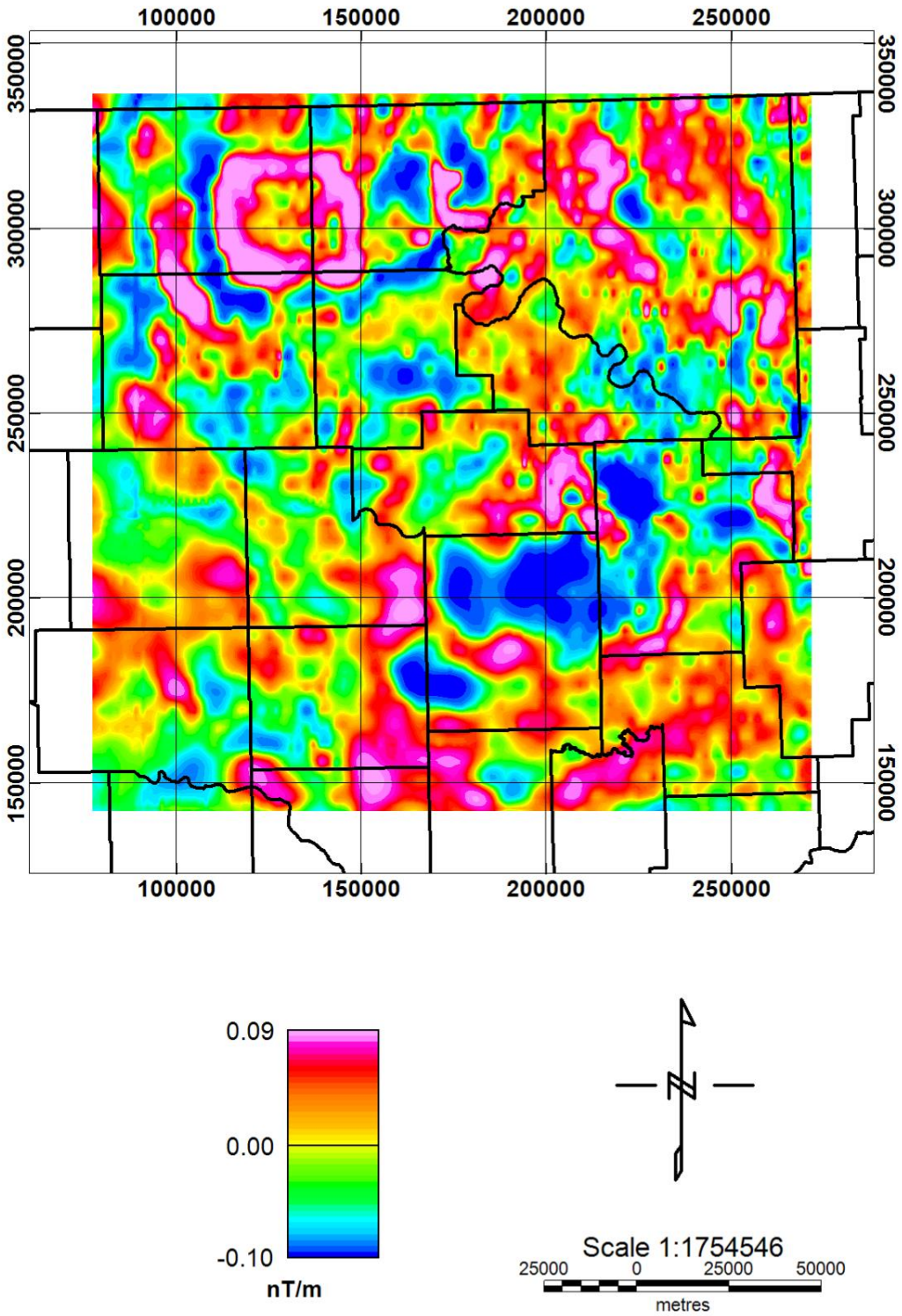

Figure A10: First vertical derivative of RTP anomaly map (Pranshu 2016).

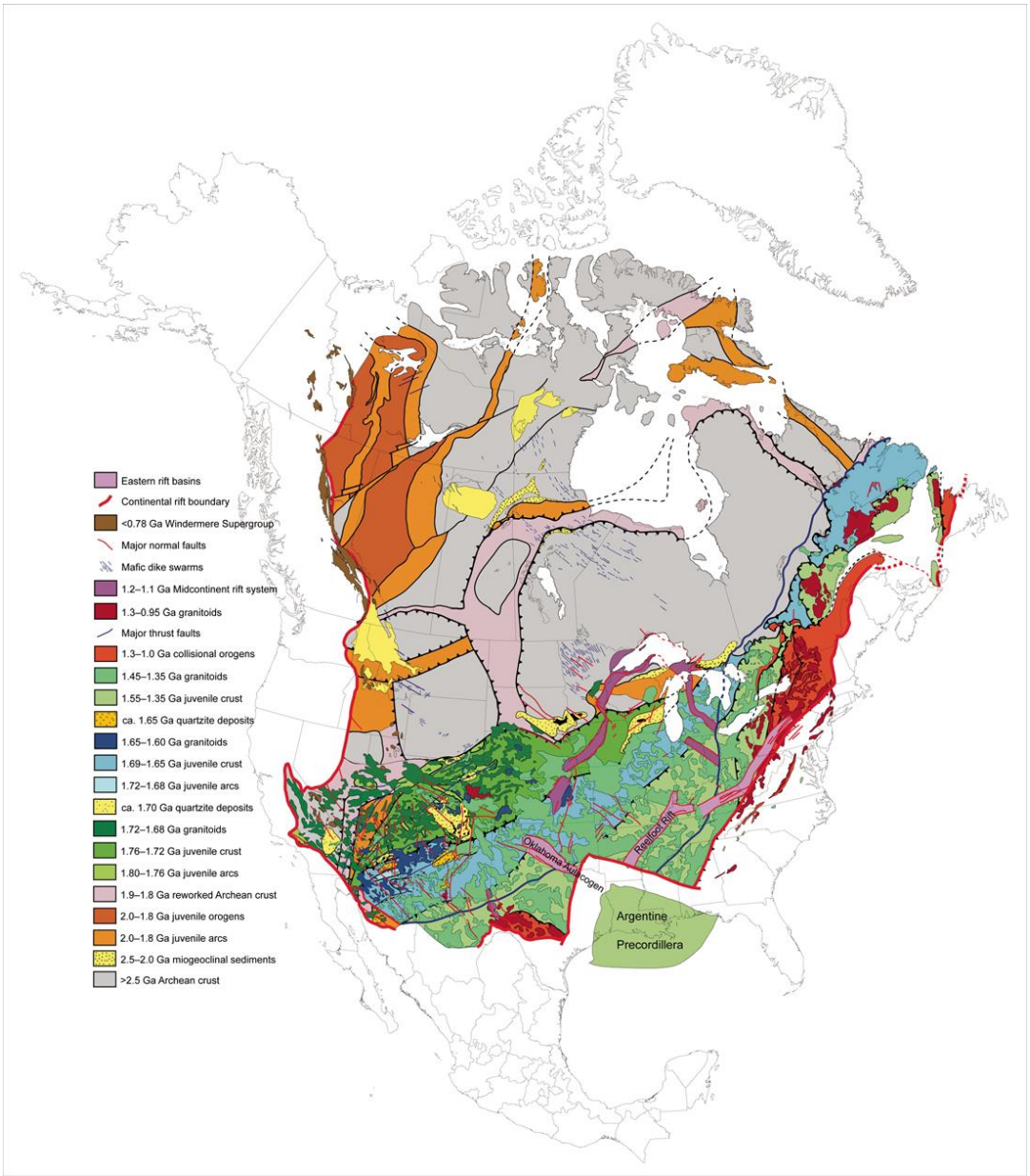

Figure A11: The final phase of eastern rifting detached the Argentine Precordillera microcontinent from the Ouachita (Texas) embayment region of southern United States (ca. 0.535 Ga). The Precordillera terrane is currently located in western Argentina. Associated failed rift arms include the Reelfoot rift and Oklahoma aulacogen (light purple). Bold red lines show rift boundaries. Whitmeyer et al. (2007).

Additional Dispersion Maps

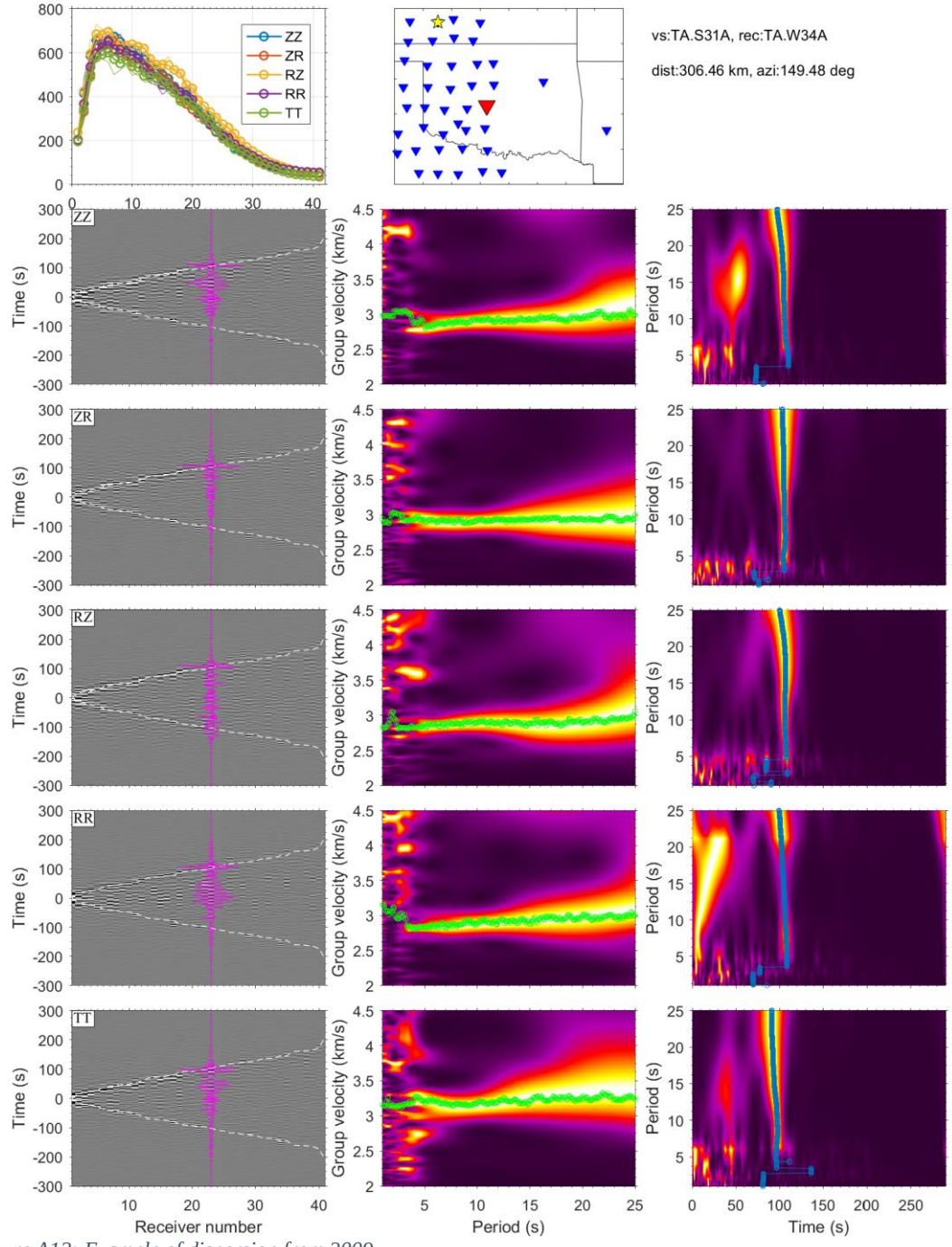

Figure A12: Example of dispersion from 2009.

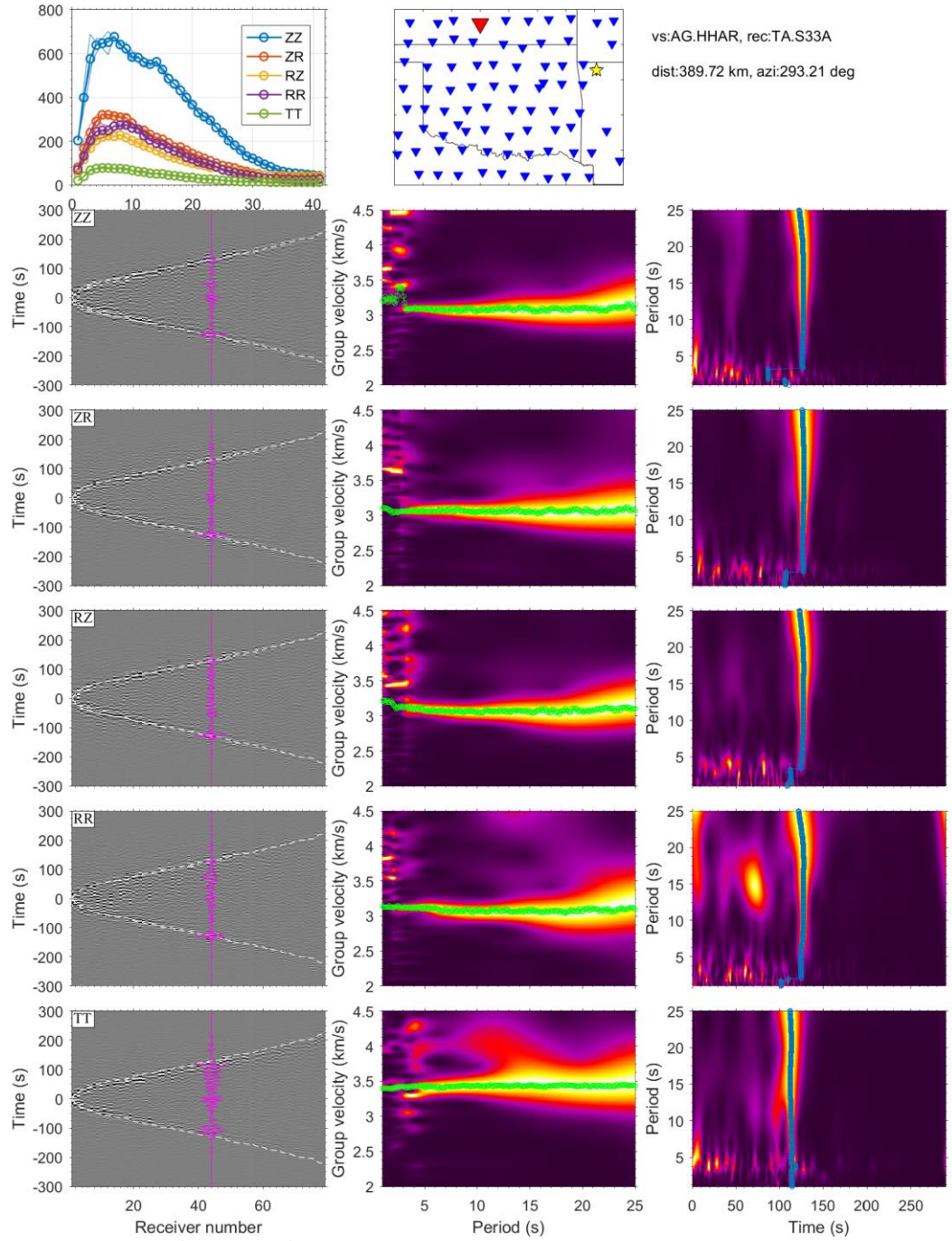

Figure A13: Example of dispersion from 2010.

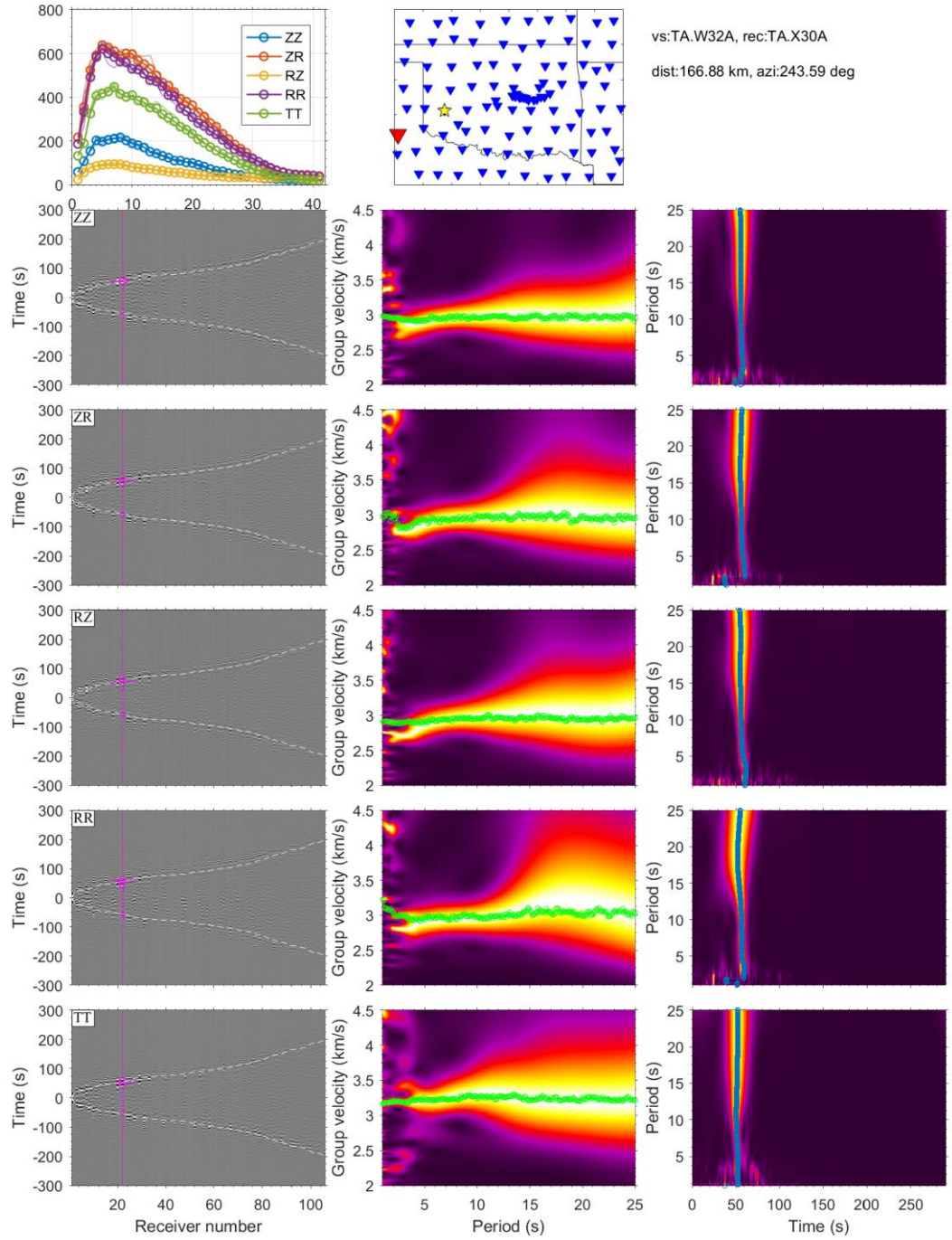

Figure A14: Example of dispersion from 2011.

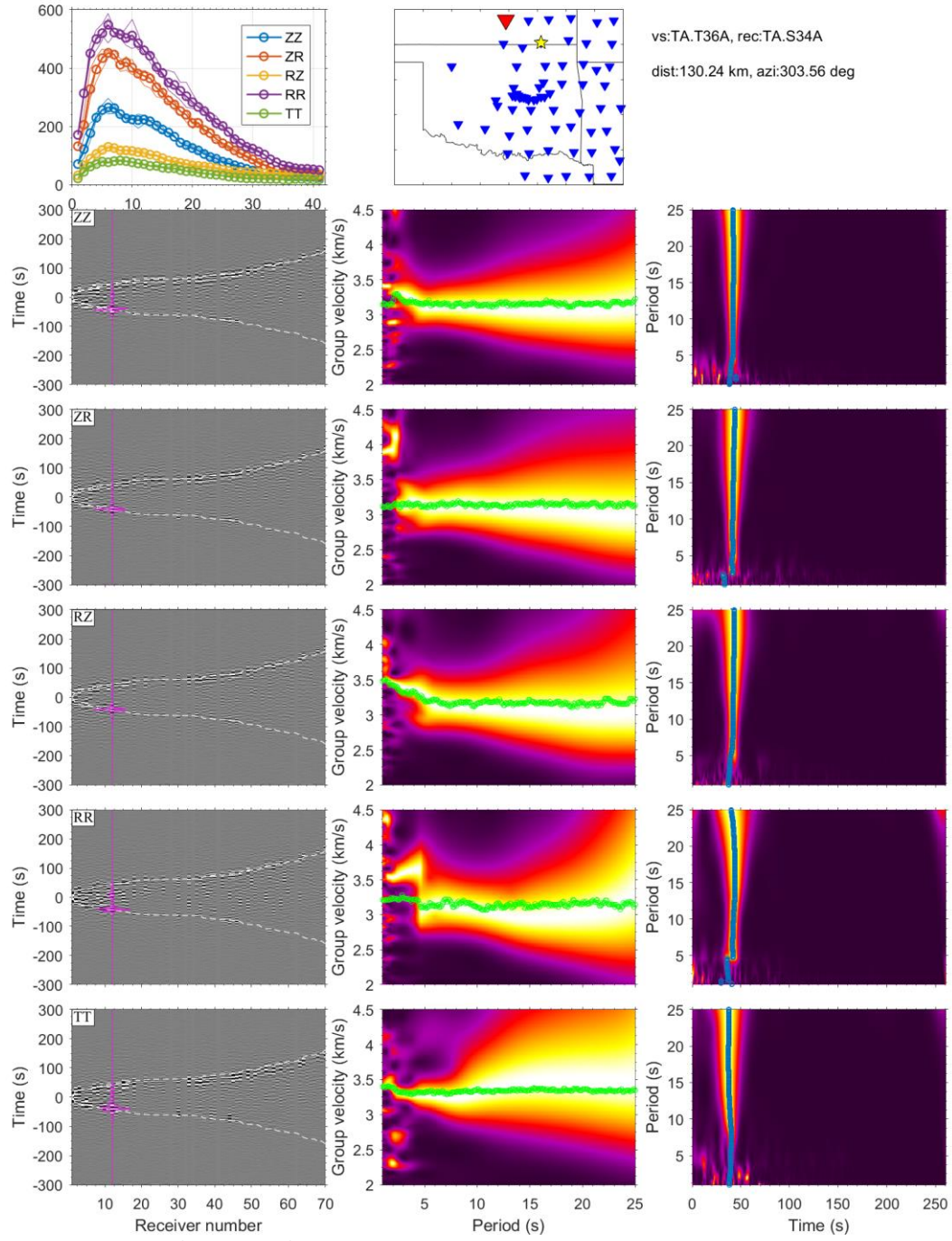

Figure A15: Example of dispersion from 2012.

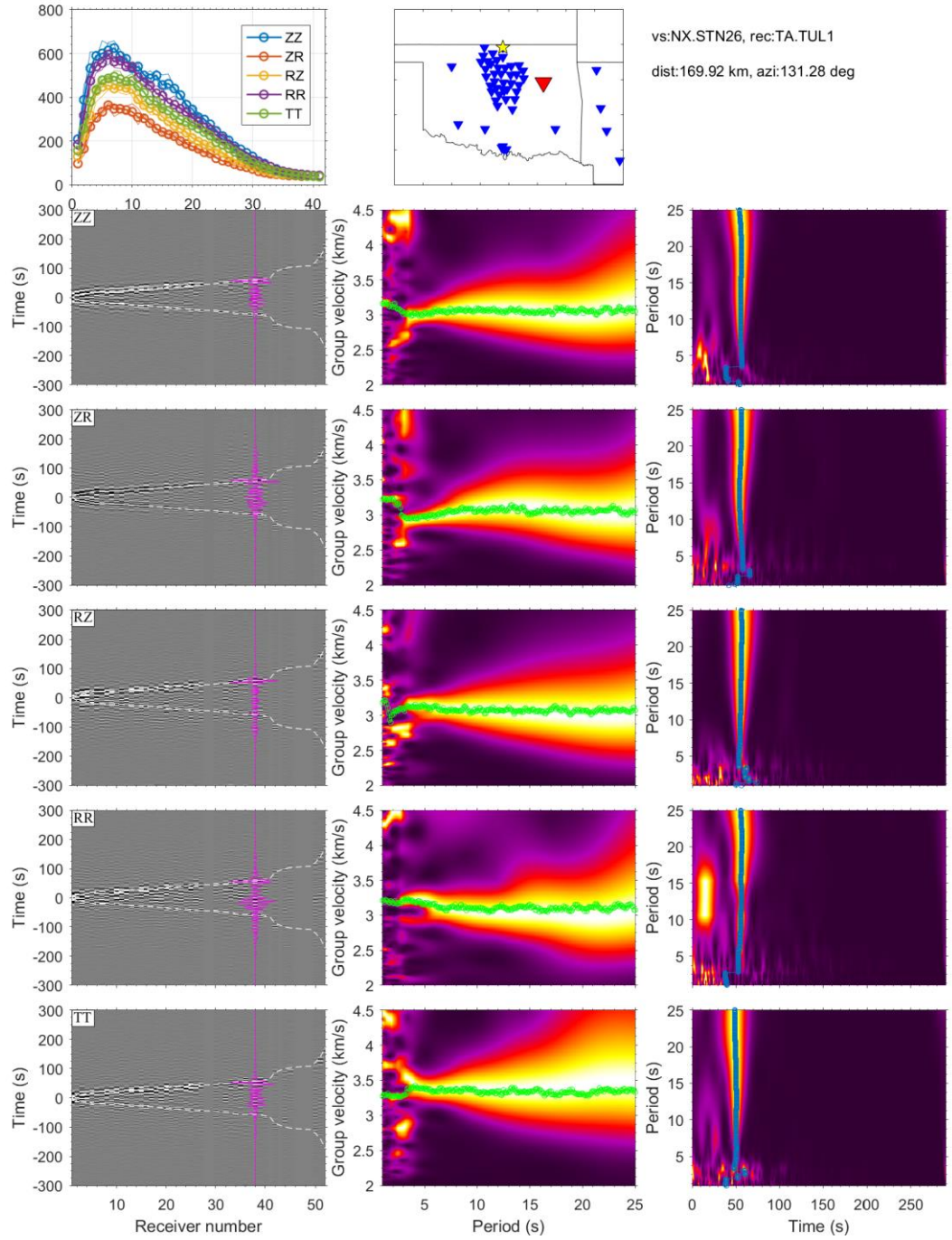

Figure A16: Example of dispersion from 2013.

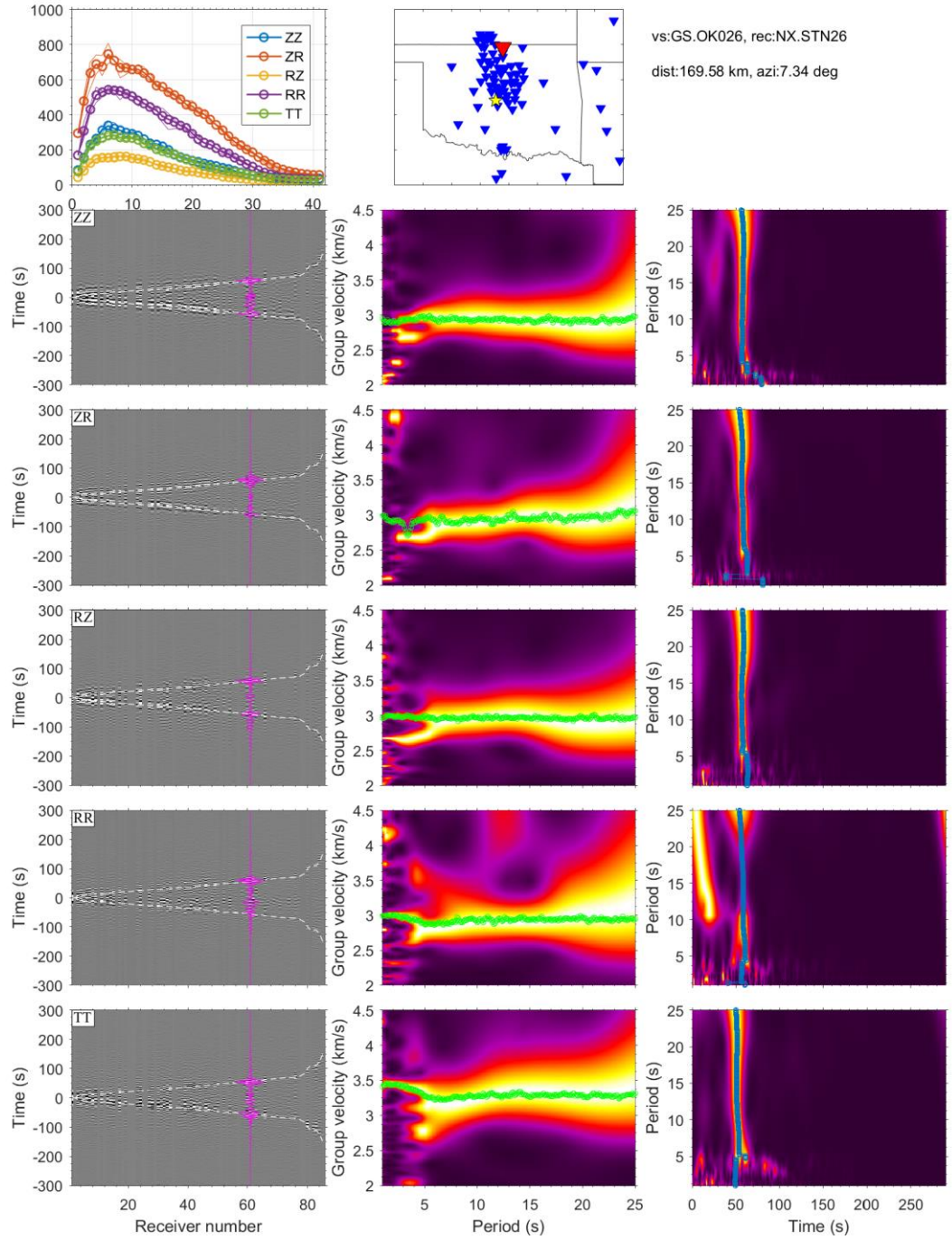

Figure A17: Example of dispersion from 2014.

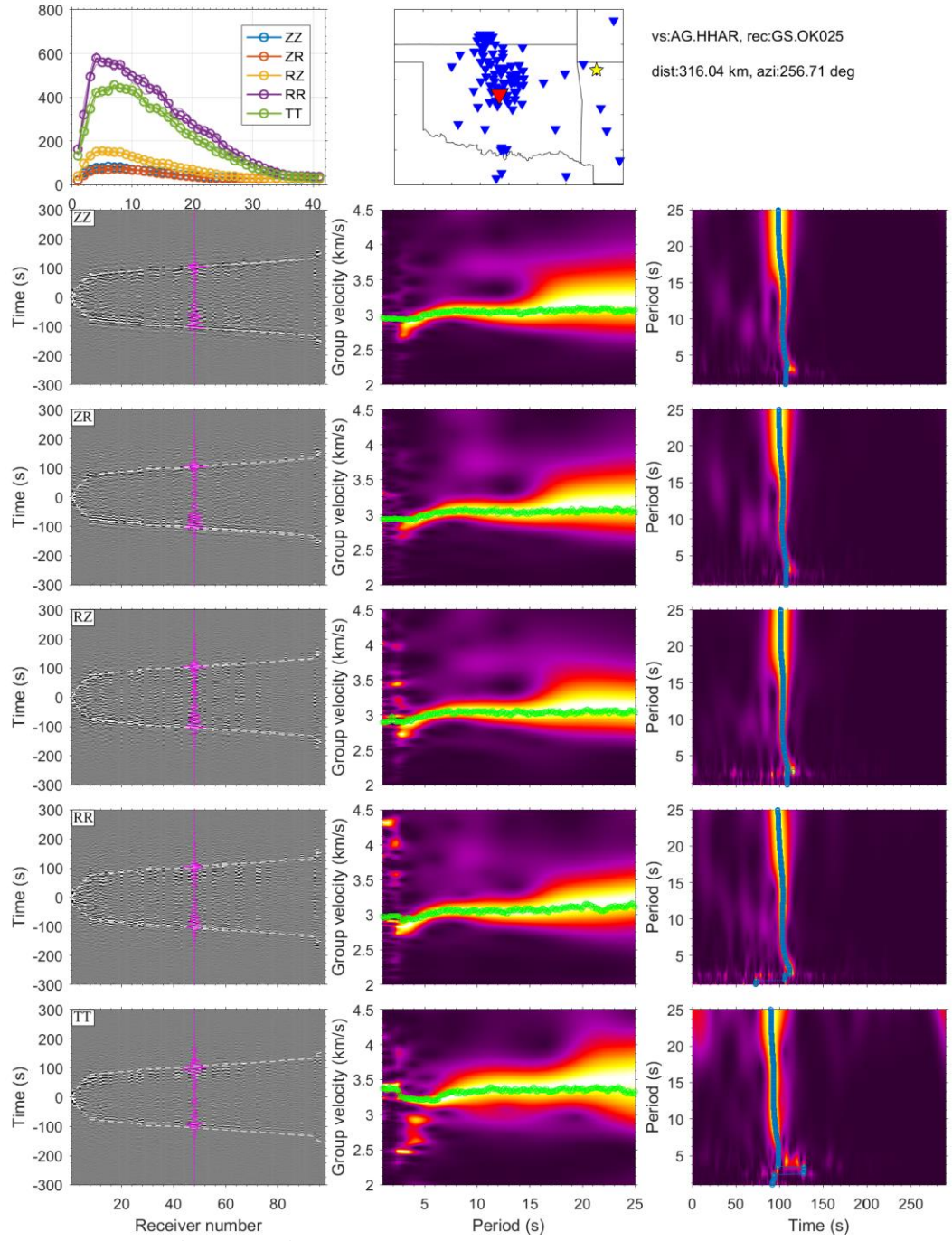

Figure A18: Example of dispersion from 2015.

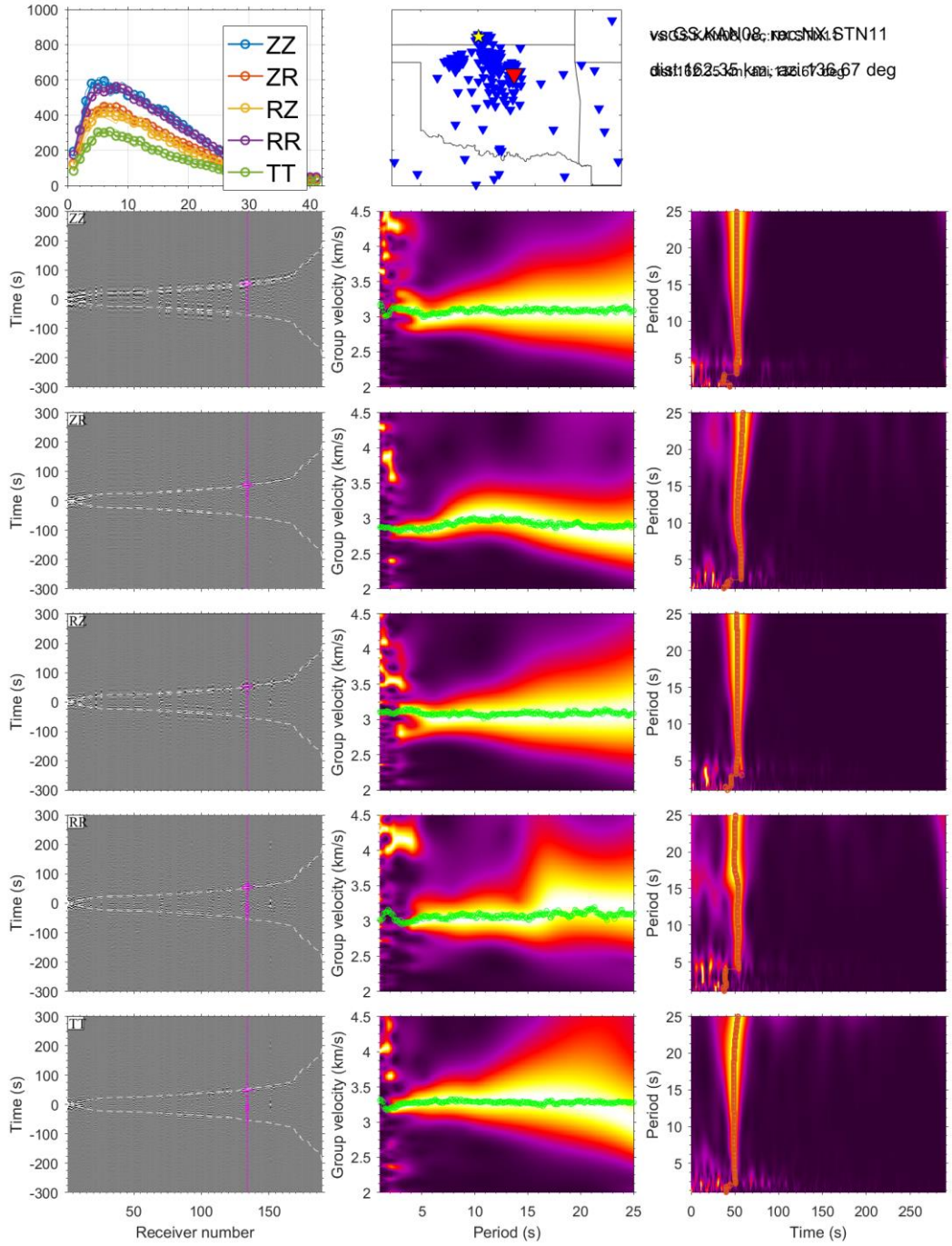

Figure A19: Example of dispersion from 2016.

Unused Tomographic Inversions

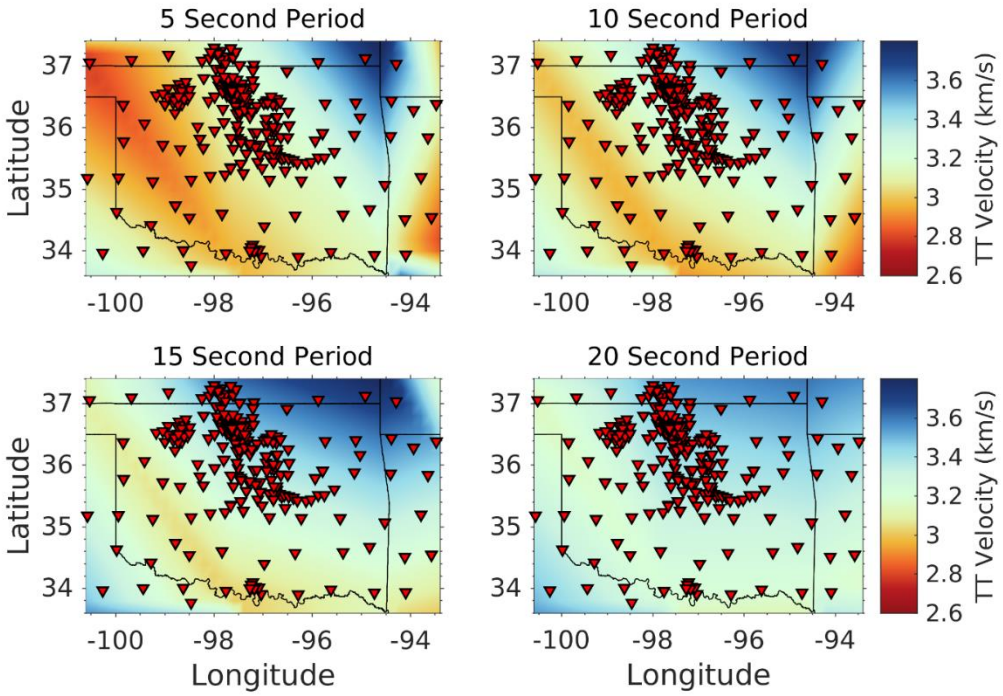

Figure A20: Example of Inversion, size of isotropic cell size 3.0.

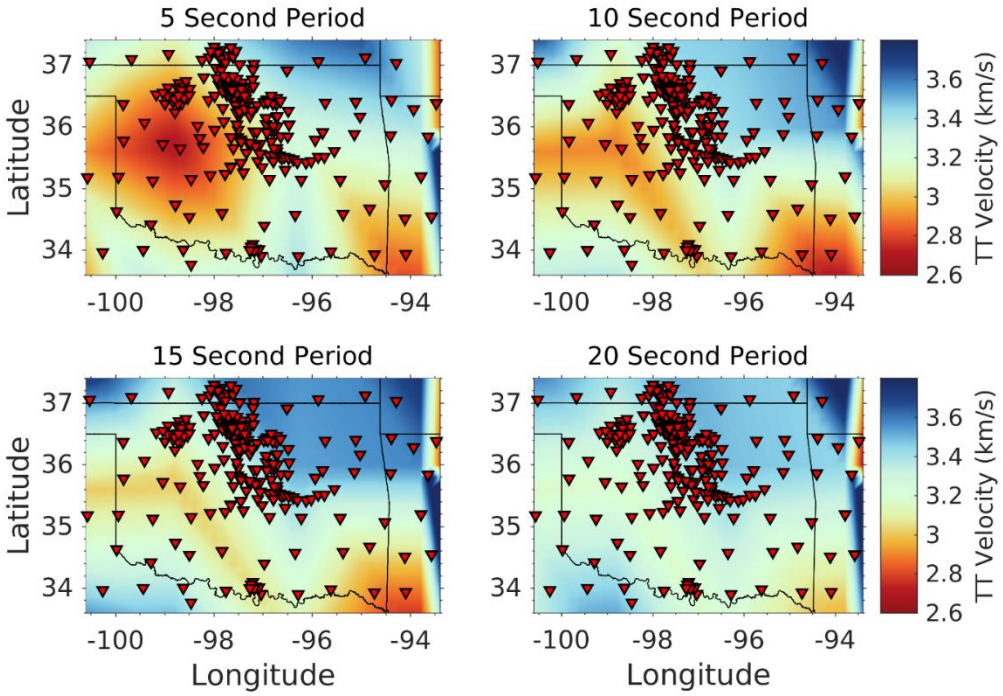

Figure A21: Example of Inversion, size of isotropic cell size 2.5.

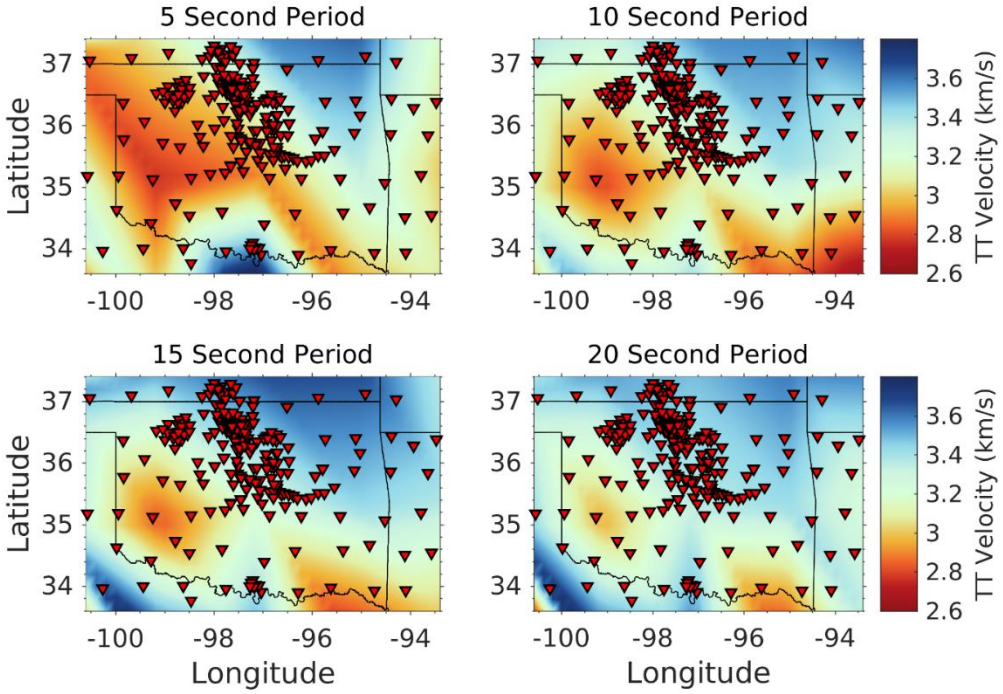

Figure A22: Example of Inversion, size of isotropic cell size 2.0.

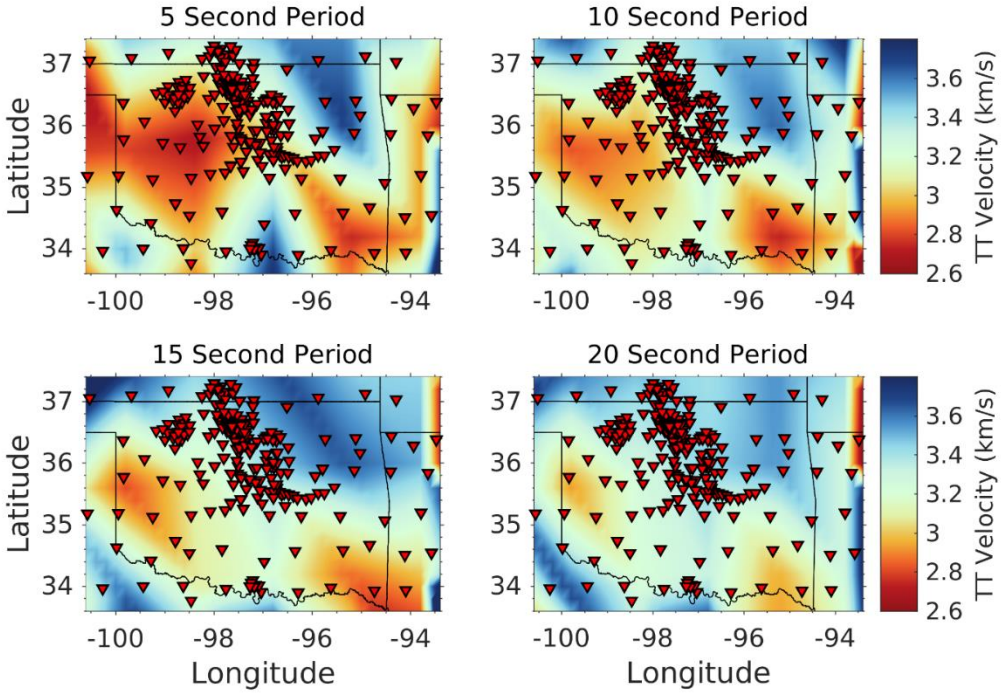

Figure A23: Example of Inversion, size of isotropic cell size 1.5.

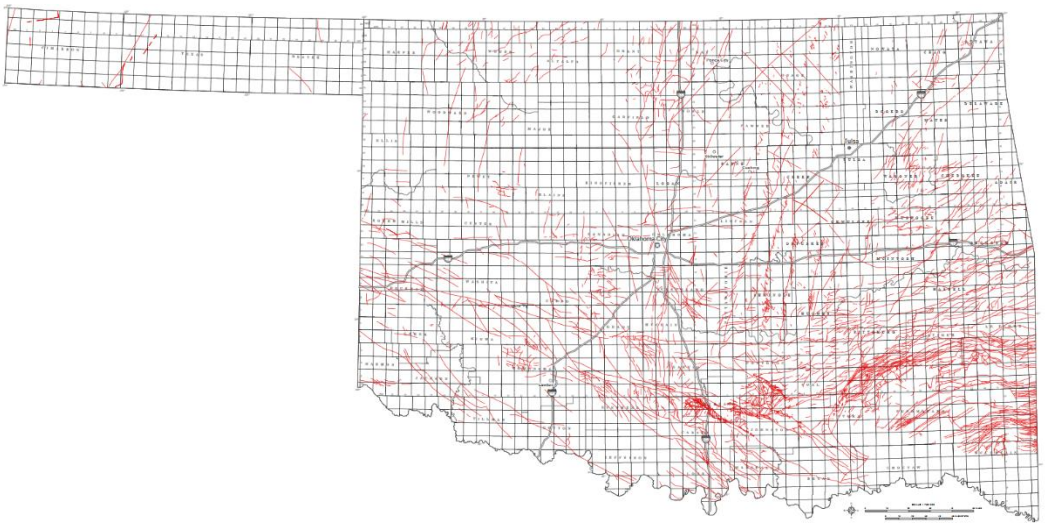

Figure A24: Interpretive Fault Map of Oklahoma. Marsh et al. (2016).